Molecular Cell

Article

RIPK1 Promotes Energy Sensing by the mTORC1 Pathway

Graphical Abstract

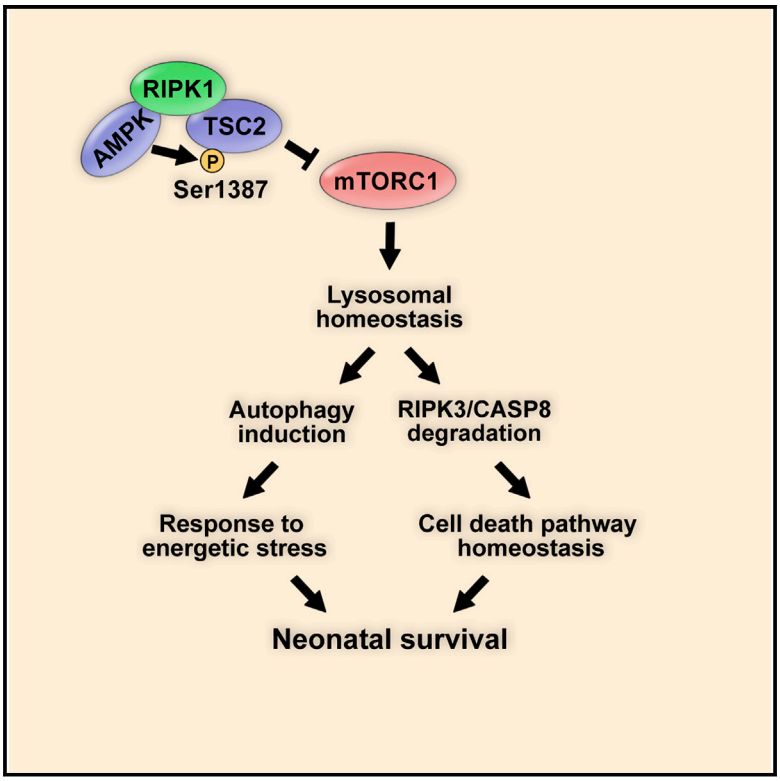

Highlights

- RIPK1 loss results in elevated mTORC1 activity, causing lysosomal dysfunction
- RIPK1 regulates mTORC1 inhibition by AMPK
- RIPK1 acts as a scaffold to promote TSC2 phosphorylation by AMPK at Ser1387
- mTORC1 inhibitor rapamycin prolongs survival of RIPK1 knockout newborn mice

Authors

Ayaz Najafov, Hoang Son Luu, Adnan K. Mookhtiar, ..., Alban Ordureau, Huibing Wang, Junying Yuan

Correspondence

ayaz_najafov@hms.harvard.edu (A.N.), jyuan@hms.harvard.edu (J.Y.)

In Brief

RIPK1 scaffold activity is known to have a pro-survival role in TNFα signaling. Najafov et al. discover an unexpected role for RIPK1 scaffold activity in mediating mTORC1 inhibition by AMPK during energetic stress. Mechanistic studies reveal that RIPK1 is involved in regulating TSC2 phosphorylation at Ser1387 by AMPK. Reduced phosphorylation of this site in RIPK1-deficient cells results in a chronically elevated mTORC1 activity and lysosomal dysfunction.

Najafov et al., 2021, Molecular Cell *81*, 1–16
January 21, 2021 © 2020 Elsevier Inc.
https://doi.org/10.1016/j.molcel.2020.11.008

CellPress

Please cite this article in press as: Najafov et al., RIPK1 Promotes Energy Sensing by the mTORC1 Pathway, Molecular Cell (2020), https://doi.org/10.1016/j.molcel.2020.11.008

Molecular Cell

CellPress

Article

RIPK1 Promotes Energy Sensing by the mTORC1 Pathway

Ayaz Najafov,[1,2,*] Hoang Son Luu,[1] Adnan K. Mookhtiar,[1] Lauren Mifflin,[1] Hong-guang Xia,[1,3] Palak P. Amin,[1] Alban Ordureau,[1] Huibing Wang,[1] and Junying Yuan[1,2,4,*]

[1]Department of Cell Biology, Harvard Medical School, Boston, MA 02115, USA

[2]Ludwig Center, Harvard Medical School, Boston, MA 02115, USA

[3]Present address: Department of Biochemistry & Research Center of Clinical Pharmacy of The First Affiliated Hospital, Zhejiang University School of Medicine, Hangzhou 310058, China

[4]Lead Contact

*Correspondence: ayaz_najafov@hms.harvard.edu (A.N.), jyuan@hms.harvard.edu (J.Y.)

https://doi.org/10.1016/j.molcel.2020.11.008

SUMMARY

The mechanisms of cellular energy sensing and AMPK-mediated mTORC1 inhibition are not fully delineated. Here, we discover that RIPK1 promotes mTORC1 inhibition during energetic stress. RIPK1 is involved in mediating the interaction between AMPK and TSC2 and facilitate TSC2 phosphorylation at Ser1387. RIPK1 loss results in a high basal mTORC1 activity that drives defective lysosomes in cells and mice, leading to accumulation of RIPK3 and CASP8 and sensitization to cell death. RIPK1-deficient cells are unable to cope with energetic stress and are vulnerable to low glucose levels and metformin. Inhibition of mTORC1 rescues the lysosomal defects and vulnerability to energetic stress and prolongs the survival of RIPK1-deficient neonatal mice. Thus, RIPK1 plays an important role in the cellular response to low energy levels and mediates AMPK-mTORC1 signaling. These findings shed light on the regulation of mTORC1 during energetic stress and unveil a point of crosstalk between pro-survival and pro-death pathways.

INTRODUCTION

The scaffold function of the receptor-interacting protein kinase 1 (RIPK1) promotes the NF-κB pathway and survival of newborn mice (Kelliher et al., 1998; Rickard et al., 2014; Silke et al., 2015). On the other hand, the catalytic activity of RIPK1 kinase promotes necroptosis and RIPK1-dependent apoptosis (Arslan and Scheidereit, 2011; Dondelinger et al., 2015; Ting and Bertrand, 2016; Wang et al., 2008). Although a kinase-inactivating mutation of RIPK1 results in no obvious phenotype (Polykratis et al., 2014), RIPK1$^{-/-}$ newborn mice do not survive past 3 days (Kelliher et al., 1998; Rickard et al., 2014; Silke et al., 2015). The neonatal lethality of RIPK1$^{-/-}$ mice has been shown to be fully rescued by double knockout of RIPK3 and CASP8, key mediators of the necroptosis and apoptosis cell death pathways, respectively (Dillon et al., 2014; Rickard et al., 2014; Silke et al., 2015). However, the mechanism behind the RIPK3/CASP8-dependent neonatal lethality induced by RIPK1 deficiency remains poorly understood. Interestingly, both RIPK3 and CASP8 have been shown to be degraded by lysosomes (Hou et al., 2010; Seo et al., 2016).

Autophagy is a lysosome-dependent catabolic pathway important for mediating cellular survival in response to starvation, stress, and infection (Dikic and Elazar, 2018; Kuma et al., 2004; Mizushima and Komatsu, 2011). The level of autophagy in mice is low during embryogenesis but is rapidly upregulated in various tissues of newborn mice before returning to basal levels within the first 1–2 days after birth (Kuma et al., 2004). Autophagy-deficient mice (e.g., Atg5$^{-/-}$) also die at the neonatal stage, similar to RIPK1$^{-/-}$ mice (Kuma et al., 2004).

Mechanistic target of rapamycin complex 1 (mTORC1) is a serine/threonine kinase complex that serves as a central nutrient-sensing hub for promoting various anabolic pathways, such as protein synthesis, and inhibiting catabolic events, such as autophagy (Hoxhaj et al., 2017; Laplante and Sabatini, 2012; Saxton and Sabatini, 2017). Overactivation of mTORC1 by expression of a constitutively active RagA$^{GTP/GTP}$ mutant leads to deficiency in autophagy and neonatal lethality (Efeyan et al., 2013). It is unclear if there may be any mechanistic connection between the neonatal lethality of RIPK1$^{-/-}$ mice and the mTORC1 or autophagy pathways.

Glucose starvation during the neonatal period activates AMPK, which inhibits mTORC1 and triggers autophagy to generate building blocks for *de novo* glucose synthesis and survival (Efeyan et al., 2013; Long et al., 2016). AMPK inhibits mTORC1 via phosphorylation of TSC2, which negatively regulates mTORC1 (Gwinn et al., 2008; Huang and Manning, 2008; Inoki et al., 2003; Shaw et al., 2004). TSC2, a GTPase-activating protein and part of the TSC complex, acts as a lysosome-associated repressor of the mTORC1 pathway (Huang and Manning, 2008; Manning et al.,

Please cite this article in press as: Najafov et al., RIPK1 Promotes Energy Sensing by the mTORC1 Pathway, Molecular Cell (2020), https://doi.org/10.1016/j.molcel.2020.11.008

2002; Menon et al., 2014; Shaw et al., 2004; Tee et al., 2002). However, how AMPK relays the information about the cellular glucose/energy levels to mTORC1 is not fully understood.

RESULTS

RIPK1 Loss Drives a Lysosomal Defect in an mTORC1-Dependent Manner

Because of the mechanistic connection of lysosomes to the neonatal lethality of autophagy-deficient and RagA$^{GTP/GTP}$ mice, and because both RIPK3 and CASP8, dual knockout of which protects RIPK1$^{-/-}$ mice from neonatal lethality, are known to be degraded by lysosomes, we examined lysosomal homeostasis in wild-type and RIPK1 knockout mouse embryonic fibroblasts (MEFs), HEK293T cells, HT-29 cells, and Jurkat cells, which were generated via CRISPR (HEK293T and HT-29 cells), homologous recombination (mice and MEFs), and chemical mutagenesis (Jurkat cells) methods (Kelliher et al., 1998; Ting et al., 1996). Strikingly, loss of RIPK1 resulted in a dramatic increase in lysosome size, decrease of lysosomal activity, as determined by cathepsin B activity with the Magic Red probe, and a decrease in lysosomal acidity, as determined by the pHrodo probe (Figures 1A–1D and S1A–S1F). Transmission electron microscopy (TEM) analysis showed that the lysosomes of the RIPK1$^{-/-}$ cells were larger in size when compared to that of wild-type cells and contained a large amount of undigested cargo (Figures 1E, S1D, and S1E).

qRT-PCR analysis revealed a dysregulated expression of the lysosomal genes upon knockout of RIPK1; although expression of several lysosomal genes did not increase (Figure S1G), the expression v-ATPase pump subunits was abnormally elevated (at non-stoichiometric ratios) (Figures 1F, S1H, and S1I), indicating a pathological dysregulation, rather than an increase in the overall lysosomal biogenesis, consistent with the aforementioned defective lysosomal phenotype (Figures 1A–1E and S1A–S1F). This dysregulation, as well as low cathepsin B activity and the lysosomal enlargement phenotype, were rescued by stable re-expression of RIPK1 (Figures S1H–S1K).

Because mTORC1 regulates the lysosomal biogenesis pathway (Peña-Llopis et al., 2011; Settembre et al., 2012), we next tested whether the dysregulated lysosomal gene expression that we discovered in RIPK1$^{-/-}$ cells was mTORC1 dependent. Importantly, we found that inhibition of mTORC1 by rapamycin or Torin-1 rescued the aberrant lysosomal gene expression, low lysosomal acidity and activity, aberrant lysosome size, and high levels of the accumulated lysosomal cargo in the RIPK1$^{-/-}$ cells (Figures 1F–1H and S1D–S1I). Consistent with this, RIPK1$^{-/-}$ cells showed high basal levels of mTORC1 pathway activity, as indicated by p-S6K Thr389, p-S6 Ser240/244, and p-ULK1 Ser757 levels (Figure 2). These findings reveal an unexpected role for RIPK1 as a negative regulator of mTORC1 activity, which, in turn, controls the lysosomal biogenesis pathway.

RIPK1 Promotes Energy Sensing and Inhibition of mTORC1 by AMPK

To inhibit mTORC1, TSC2 integrates inputs from various pathways, including growth factor-stimulated pathways mediated by Akt, as well as metabolic and environmental stress inputs from AMPK (Huang and Manning, 2008). We found that Akt-dependent mTORC1 activity was not significantly affected by the loss of RIPK1 because inhibition of mTORC1 signaling by Akt inhibitor MK-2206 was equally effective in wild-type and RIPK1$^{-/-}$ cells (Figure 3A). Similarly, RIPK1 loss did not affect the inhibition of mTORC1 activity following rapamycin or Torin-1 treatment (Figure 3A). Moreover, inhibition of mTORC1 in response to amino acid deprivation was also not significantly affected in RIPK1$^{-/-}$ cells, suggesting that RIPK1 is not involved in the regulation of the v-ATPase-Ragulator-Rag-mTORC1 pathway (Efeyan et al., 2012), which is responsible for sensing cellular amino acid levels (Figures 3B and 3C). Consistent with these results, the lysosomal localization of mTOR, as well as the cytosolic localization of TSC2, was not affected by the loss of RIPK1 (Figure S2).

On the other hand, remarkably, we found that activation of AMPK resulted in potent inhibition of mTORC1 signaling in wild-type, but not RIPK1$^{-/-}$, cells, as judged by phosphorylation of S6K, S6, and a mobility shift of 4EBP1, in response to glucose starvation (Hardie, 2011) or AMP-mimic agent AICAR (Sullivan et al., 1994) treatment (Figures 3D and 3E). The extent of AMPK activation was comparable in wild-type and RIPK1$^{-/-}$ cells, as judged by phosphorylation levels of ACC, an AMPK substrate (Figures 3D and 3E). Such compromised mTORC1 inhibition phenotype was also observed when the constitutively active AMPK^{T172D} mutant was expressed in wild-type versus RIPK1$^{-/-}$ cells, suggesting that the inability of the RIPK1$^{-/-}$ cells to inhibit mTORC1 in response to AMPK activation is due to a defect downstream of AMPK (Figure S3A).

Defective mTORC1 inhibition following AMPK activation in RIPK1$^{-/-}$ cells was also observed when AMPK was activated by treatment with A-769662 (a direct AMPK agonist) (Cool et al., 2006), AMP-boosting compounds 2-DG, metformin, or CCCP (Hardie et al., 2012) (Figures S3B–S3F). Defective inhibition of mTORC1 upon glucose starvation was also observed in the AMPKα1$^{-/-}$/α2$^{-/-}$ MEF cells, consistent with the notion that RIPK1$^{-/-}$ cells may have a compromised signal relay between AMPK and mTORC1 (Figure S3G).

Importantly, mTORC1 inhibition downstream of AMPK activation was not compromised upon treatment of wild-type cells with RIPK1 inhibitor Nec-1s or in RIPK3$^{-/-}$, MLKL$^{-/-}$, XIAP$^{-/-}$, cIAP1/2$^{-/-}$, NEMO$^{-/-}$, or p65$^{-/-}$/p50$^{-/-}$ MEFs (Figures S4A–S4C). Additionally, double knockout of RIPK3 and CASP8 did not rescue the compromised mTORC1 inhibition downstream of AMPK activation and the dysregulated lysosomal gene expression in RIPK1$^{-/-}$ cells (Figures S4D and S4E). Therefore, the non-catalytic, scaffold function of RIPK1 is involved in promoting the sensing of the cellular energy levels by the AMPK-mTORC1 pathway independent of the RIPK1-interacting TNFα receptor signaling components, the NF-κB pathway, and the RIPK3/CASP8 pro-death pathways.

Consistent with the cellular requirement for RIPK1 to mediate a normal response to AMPK activation, the proliferation of the RIPK1$^{-/-}$ cells was strongly sensitized to glucose deprivation or metformin treatment (Figure 3F). On the other hand, RIPK1$^{-/-}$ cells were not strongly sensitized to direct mTORC1 inhibition by rapamycin, Torin-1, or inhibition of growth factor signaling inputs

Please cite this article in press as: Najafov et al., RIPK1 Promotes Energy Sensing by the mTORC1 Pathway, Molecular Cell (2020), https://doi.org/10.1016/j.molcel.2020.11.008

CellPress

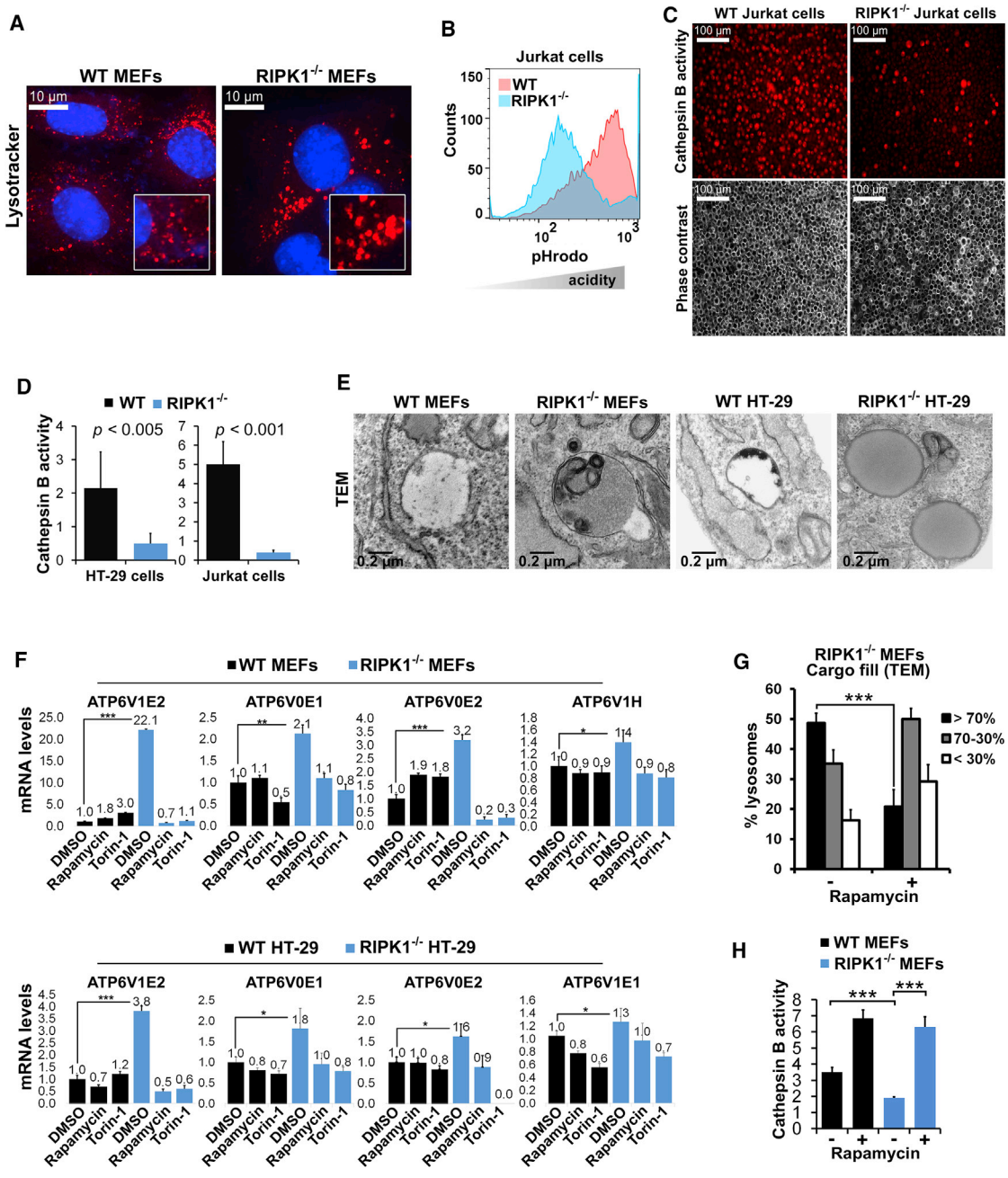

Figure 1. RIPK1 Loss Promotes Lysosomal Dysfunction Downstream of mTORC1

(A) Enlargement of lysosomes in RIPK1$^{-/-}$ MEFs. Cells were stained with LysoTracker and DAPI and analyzed by fluorescence microscopy.

(B) Lysosomal pH defect in RIPK1$^{-/-}$ Jurkat cells. Cells were stained with pHrodo and analyzed by flow cytometry.

(C) Lysosomal activity defect in RIPK1$^{-/-}$ Jurkat cells. Live cells were stained with Magic Red cathepsin B activity probe and analyzed by fluorescence and phase contrast microscopy.

(D) Lysosomal activity defect in RIPK1$^{-/-}$ HT-29 and Jurkat cells, as determined by Magic Red.

(E) Lysosomal cargo digestion defect in RIPK1$^{-/-}$ MEFs and HT-29 cells, as determined by transmission electron microscopy (TEM).

(F) mTORC1-dependent lysosomal biogenesis gene expression dysregulation in RIPK1$^{-/-}$ cells. Cells were treated with either rapamycin or Torin-1 for 16 h, and lysosomal gene expression was analyzed by qRT-PCR.

(G) Lysosomal cargo digestion defect in RIPK1$^{-/-}$ MEFs can be rescued by a 16 h rapamycin treatment. Lysosomes were divided into three categories according to the extent of how filled with cargo they appear and scored with TEM.

(H) Lysosomal activity (cathepsin B) defect in RIPK1$^{-/-}$ MEFs can be rescued by a 16 h rapamycin treatment.

*p < 0.05, **p < 0.01, ***p < 0.001. Mean and SEM are plotted.

Please cite this article in press as: Najafov et al., RIPK1 Promotes Energy Sensing by the mTORC1 Pathway, Molecular Cell (2020), https://doi.org/10.1016/j.molcel.2020.11.008

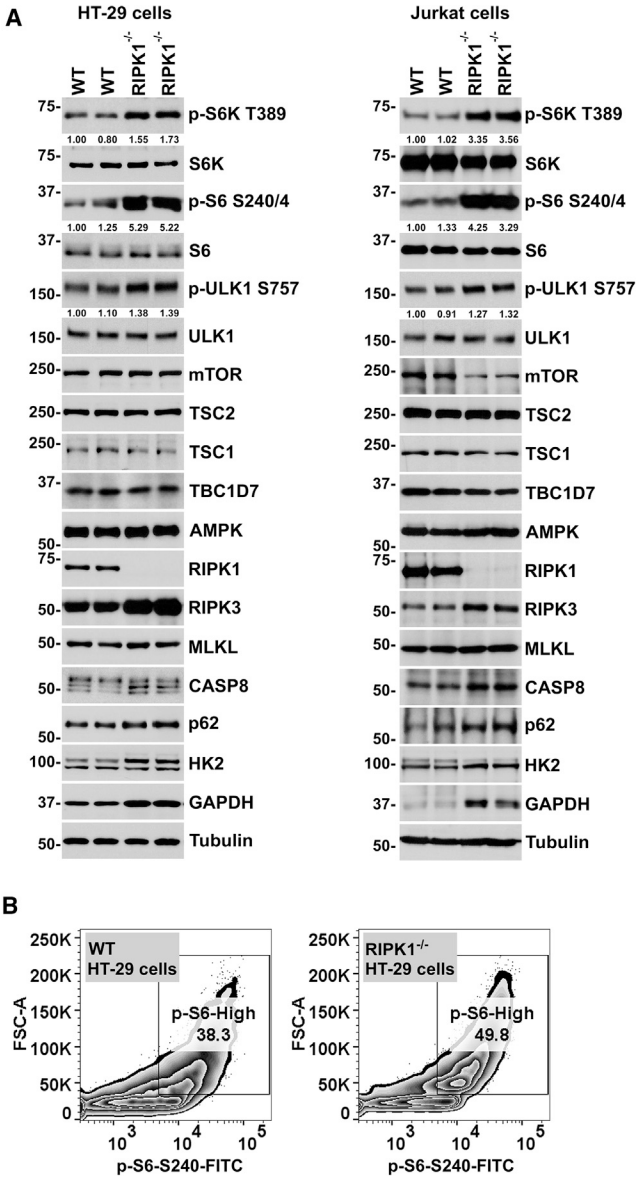

Figure 2. RIPK1 Loss Results in Elevation of the Basal mTORC1 Pathway Activity and the Accumulation of Lysosomal Substrates

(A) Elevated basal mTORC1 pathway activity, accumulation of RIPK3/CASP8, and lysosomal substrates HK2 and GAPDH in RIPK1$^{-/-}$ HT-29 cells and RIPK1-deficient Jurkat cells. Cell lysates were immunoblotted with indicated antibodies. The values under the blots indicate phospho/total quantification of the bands with respect to the first lane.

(B) Elevated basal mTORC1 pathway activity in RIPK1$^{-/-}$ cells as judged by flow cytometry. Indicated HT-29 cells were stained for p-S6-FITC and analyzed by flow cytometry. The gates and the percentages of gated cell populations are indicated.

into the mTORC1 pathway by treatment with the Akt inhibitor MK-2206 or the PI3K inhibitor GDC-0941 (Figures 3F and S4F).

Overall, these results suggest that the scaffold function of RIPK1 is required to relay the information about cellular energy status, but not that of growth factors or cellular amino acid levels, to inhibit mTORC1 downstream of AMPK activation. Moreover, these results place RIPK1 as an important mediator of cell survival during cellular stress resulting from energy deprivation.

RIPK1 Promotes AMPK-Mediated TSC2 Activation and mTORC1 Inhibition

TSC2 is one of the main inputs from AMPK into the mTORC1 pathway, and the loss of TSC2 has been shown to block mTORC1 inhibition upon AMPK activation (Inoki et al., 2003) in a fashion similar to what we found in RIPK1$^{-/-}$ cells (Figures S5A and S5B). Moreover, TSC2 phosphorylation by AMPK at Ser1387 has been shown to be important for the inhibition of mTORC1 downstream of glucose/energy deprivation (Gwinn et al., 2008; Huang and Manning, 2008; Inoki et al., 2003; Shaw et al., 2004). Thus, we next analyzed whether TSC2 plays a role downstream of RIPK1 in mediating the AMPK activation signal to mTORC1. Consistent with the observation that mTORC1 inhibition downstream of AMPK activation is defective in the absence of RIPK1, we found that the phosphorylation of TSC2 at Ser1387 was strongly diminished in RIPK1$^{-/-}$ cells upon AMPK activation, following either metformin treatment, glucose starvation, or treatment with AMPK activator A-769662, similar to results seen in AMPKα1$^{-/-}$/α2$^{-/-}$ MEF cells (Figures 3D and 3E, 4A–4C, and S5C).

In addition to the TSC2 input, AMPK impinges on the mTORC1 pathway via phosphorylation of mTORC1 subunit Raptor at Ser792 (Gwinn et al., 2008). We found that Raptor p-S792 levels were not affected in RIPK1$^{-/-}$ cells upon AMPK activation, unlike TSC2 p-S1387 levels (Figure S5D), which is consistent with the notion that the role of RIPK1 is to mediate AMPK-TSC2 interaction and not activation of AMPK. Additionally, our western blotting data using a pan-AMPK substrate phospho-specific motif antibody also suggest that RIPK1 loss does not affect the global phosphorylation of AMPK targets but has a TSC2-specific effect, as the proposed scaffold role suggests (Figure S5E).

Importantly, endogenous AMPK and TSC2 interacted with endogenous RIPK1 upon AMPK activation (Figures 4B–4D), and AMPK-TSC2 interaction was not induced following AMPK activation in the absence of RIPK1 expression (Figure 4E). AMPK weakly interacted with TSC2 prior to glucose starvation in both wild-type and RIPK1$^{-/-}$ cells; however, following glucose starvation, the AMPK-TSC2 interaction was induced only in the presence of RIPK1 expression (Figure 4E). Furthermore, the direct interaction of separately purified RIPK1 and AMPK, as well as RIPK1 and TSC2, could be detected *in vitro* (Figures 4F and 4G).

Because RIPK1$^{-/-}$ cells demonstrate diminished TSC2 Ser1387 phosphorylation induction upon AMPK activation and a lack of mTORC1 inhibition, we employed CRISPR/cas9-induced knock-in of the S1387E phospho-mimic mutation to rescue this mTORC1 phenotype because S1387E mutation would mimic the effect of AMPK activation on TSC2 and suppress mTORC1, independent of the ability of AMPK to phosphorylate TSC2. Notably, unlike HEK293T-RIPK1$^{-/-}$ cells, where glucose starvation did not result in mTORC1 inhibition, two distinct HEK293T-RIPK1$^{-/-}$;TSC2$^{+/S1387E}$ heterozygous knock-in clones (Figure S6A) had lower basal mTORC1 activity levels and responded to AMPK activation by glucose starvation similar to that of wild-type cells, in terms of mTORC1 inhibition

Please cite this article in press as: Najafov et al., RIPK1 Promotes Energy Sensing by the mTORC1 Pathway, Molecular Cell (2020), https://doi.org/10.1016/j.molcel.2020.11.008

CellPress

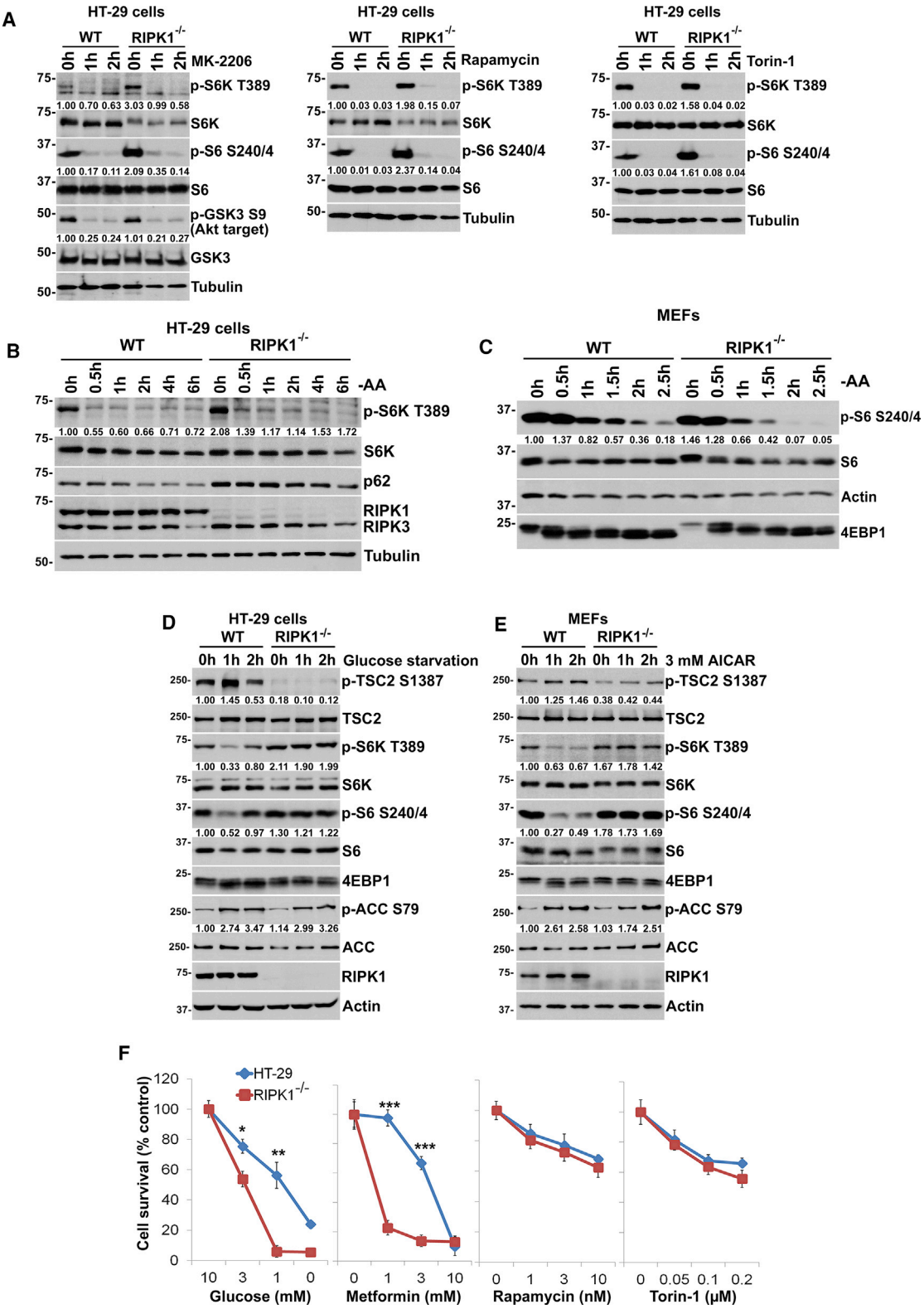

Figure 3. RIPK1 Promotes Cellular Energy Level Sensing and Inhibition of mTORC1 by AMPK

(A) Lack of differential inhibition of mTORC1 signaling in wild-type versus RIPK1$^{-/-}$ HT-29 cells upon inhibition of Akt by MK-2206 and mTORC1 by rapamycin or Torin-1. Cells were treated for indicated time points, and cell lysates were immunoblotted with indicated antibodies.

(legend continued on next page)

Please cite this article in press as: Najafov et al., RIPK1 Promotes Energy Sensing by the mTORC1 Pathway, Molecular Cell (2020), https://doi.org/10.1016/j.molcel.2020.11.008

(Figure 4H). Similar results were observed upon knock-in of the S1387E mutation into RIPK1$^{-/-}$ HT-29 cells (Figures S6A–S6C). Moreover, the dysregulated lysosomal gene expression levels and low cathepsin B activity levels were also significantly rescued by the S1387E knock-in (Figures 4I and 4J). Lastly, the sensitivity of RIPK1$^{-/-}$ cells to low energy levels, in terms of cell growth, was also rescued by the S1387E knock-in (Figures 4K and 4L).

Transfection of the RIPK1^{K45M} kinase-dead mutant promoted AMPK-TSC2 interaction, further confirming the notion of a non-catalytic, scaffold role for RIPK1 in promoting AMPK-TSC2 interaction (Figure 5A). The deletion of the RIPK1 C-terminal region (aa 289-end), which includes the death domain (DD) and the intermediate domain (ID), enhanced the interaction of RIPK1 with AMPK/TSC2, while deletion of the DD alone did not give this effect (Figure 5B). Additionally, deletion of the kinase domain (aa 1-275) did not block the RIPK1 interaction with AMPK/TSC2, suggesting that the ID can also bind with AMPK/TSC2 (Figure 5B). However, the 3D structure of the complex needs to be solved to fully understand these interactions.

We found that overexpression of a catalytically inactive mutant RIPK1^{K45M} was sufficient to promote mTORC1 inhibition and inhibit the dysregulated expression of the lysosomal genes (Figures 5C and 5D). On the other hand, overexpression of constitutively active AMPK^{T172D} could not suppress the elevated lysosomal gene expression in RIPK1$^{-/-}$ cells (Figure 5D), consistent with the findings shown in Figure S3A, where AMPK^{T172D} expression could not inhibit mTORC1 in the absence of RIPK1.

In agreement with our knowledge of the RIPK1 scaffold function in the TNFα signaling, where RIPK1 ubiquitination plays a key role in promoting survival (Christofferson et al., 2014; Ofengeim and Yuan, 2013), glucose starvation also resulted in ubiquitination of RIPK1 via K63-linked, but not K48-linked or M1-linked, chains, as determined by immunoprecipitation of endogenous RIPK1 via ubiquitin chain-specific 3 M urea-resistant nanobodies (Figure 5E). Notably, RIPK1-AMPK-TSC2 formed a ternary complex, as determined by tandem immunoprecipitation experiments (Figure 5F). Finally, supplementing purified RIPK1^{K45M} into an *in vitro* kinase reaction, where AMPK^{T172D} was used as a kinase and TSC2 as a substrate, enhanced TSC2 phosphorylation at S1387 (Figures 5G and 5H).

Transient treatment of RIPK1$^{-/-}$ cells with rapamycin rescued their sensitivity to low energy and glucose levels (Figure S6D). This is also consistent with the ability of mTORC1 inhibition to restore lysosomal function in RIPK1$^{-/-}$ cells (Figures 1F–1H and S1D–S1I), since the restoration of normal lysosomal function would allow cells to respond to such energetic stresses by inducing autophagy and synthesizing glucose *de novo*, from amino acids.

Taken together, these results demonstrate that the scaffold function of RIPK1 promotes AMPK-mediated phosphorylation of TSC2 Ser1387 (Figure S6E), which in turn leads to mTORC1 inhibition upon energy deprivation in order to promote lysosomal biogenesis and autophagy for replenishing the cellular glucose/energy levels. The proposed mechanism is in complete accord with the original finding by Inoki et al. that TSC2 phosphorylation by AMPK at Ser1387 is critical for mTORC1 inhibition during energetic stress (note that Inoki et al. employed rat TSC2, where human Ser1387 residue corresponds to rat Ser1345) (Inoki et al., 2003). Consistent with this model, the lysosomal localization of mTOR, as well as the cytosolic localization of TSC2, was not affected by the loss of RIPK1 following glucose starvation (Figure S2).

RIPK1 Loss in Mice Drives Overactivation of mTORC1, Lysosomal Defects, and Accumulation of RIPK3 and CASP8

The large intestine shows one of the strongest cell death phenotypes in RIPK1$^{-/-}$ mice and the lethality of the neonatal pups has been proposed to be, at least partially because of damaged intestinal structure and starvation, due to nutrient absorption failure (Dannappel et al., 2014; Dillon et al., 2014; Rickard et al., 2014; Silke et al., 2015; Takahashi et al., 2012). Thus, our subsequent experiments were focused on the large intestinal tissues of the RIPK1$^{-/-}$ neonatal mice.

Consistent with the observations made in the MEFs, HT-29, HEK293T, and Jurkat cells, the large intestines of neonatal RIPK1$^{-/-}$ mice also demonstrated elevated mTORC1 activity, as indicated by increased p-S6K and p-S6, as well as dysregulated lysosomal gene expression, larger and defective lysosomes (as judged by TEM and Cathepsin B activity, respectively), and increased levels of p62 and HK2, indicative of compromised lysosomal degradation capacity (Figures 6A–6D). Compared to intestines, a less pronounced lysosomal gene expression dysregulation and elevated mTORC1 activity levels were found in neonatal RIPK1$^{-/-}$ liver, lungs, and heart tissues and minimal or no changes were found in the brain tissue (Figures S7A and S7B). Similar to our observations in RIPK1$^{-/-}$ cells, v-ATPase subunits were overexpressed in RIPK1$^{-/-}$ tissues at non-stoichiometric ratios (Figure S7A), while other lysosomal biogenesis gene expression levels were not increased (Figure S7C), consistent with the notion that RIPK1 loss results in a dysregulation of lysosomal function rather than an overall

(B) Lack of differential inhibition of mTORC1 signaling in wild-type versus RIPK1$^{-/-}$ HT-29 cells upon amino acid starvation. Cells were treated with dialyzed FBS-containing HBSS medium supplemented with glucose for the indicated time points, and cell lysates were immunoblotted with indicated antibodies.
(C) As in (B), except wild-type versus RIPK1$^{-/-}$ MEFs were used.
(D) Compromised glucose sensing and inhibition of mTORC1 in RIPK1$^{-/-}$ HT-29 cells. Cells were glucose starved for indicated time points, and cell lysates were immunoblotted with indicated antibodies.
(E) Defective mTORC1 inhibition in RIPK1$^{-/-}$ MEFs following activation of AMPK by AICAR. Cells were treated with AICAR for indicated time points, and cell lysates were immunoblotted with indicated antibodies.
(F) Defective survival at low glucose/energy levels with no change in sensitivity to mTORC1 and mTOR inhibition in RIPK1$^{-/-}$ HT-29 cells. Cells were treated with indicated concentrations of glucose in glucose-free medium or metformin, rapamycin, or Torin-1 in normal medium, and cell growth was analyzed by crystal violet staining 72 h later. *$p < 0.05$, **$p < 0.01$, ***$p < 0.001$. Mean and SEM are plotted. The values under the blots indicate phospho/total quantification of the bands with respect to the first lane.

Please cite this article in press as: Najafov et al., RIPK1 Promotes Energy Sensing by the mTORC1 Pathway, Molecular Cell (2020), https://doi.org/10.1016/j.molcel.2020.11.008

CellPress

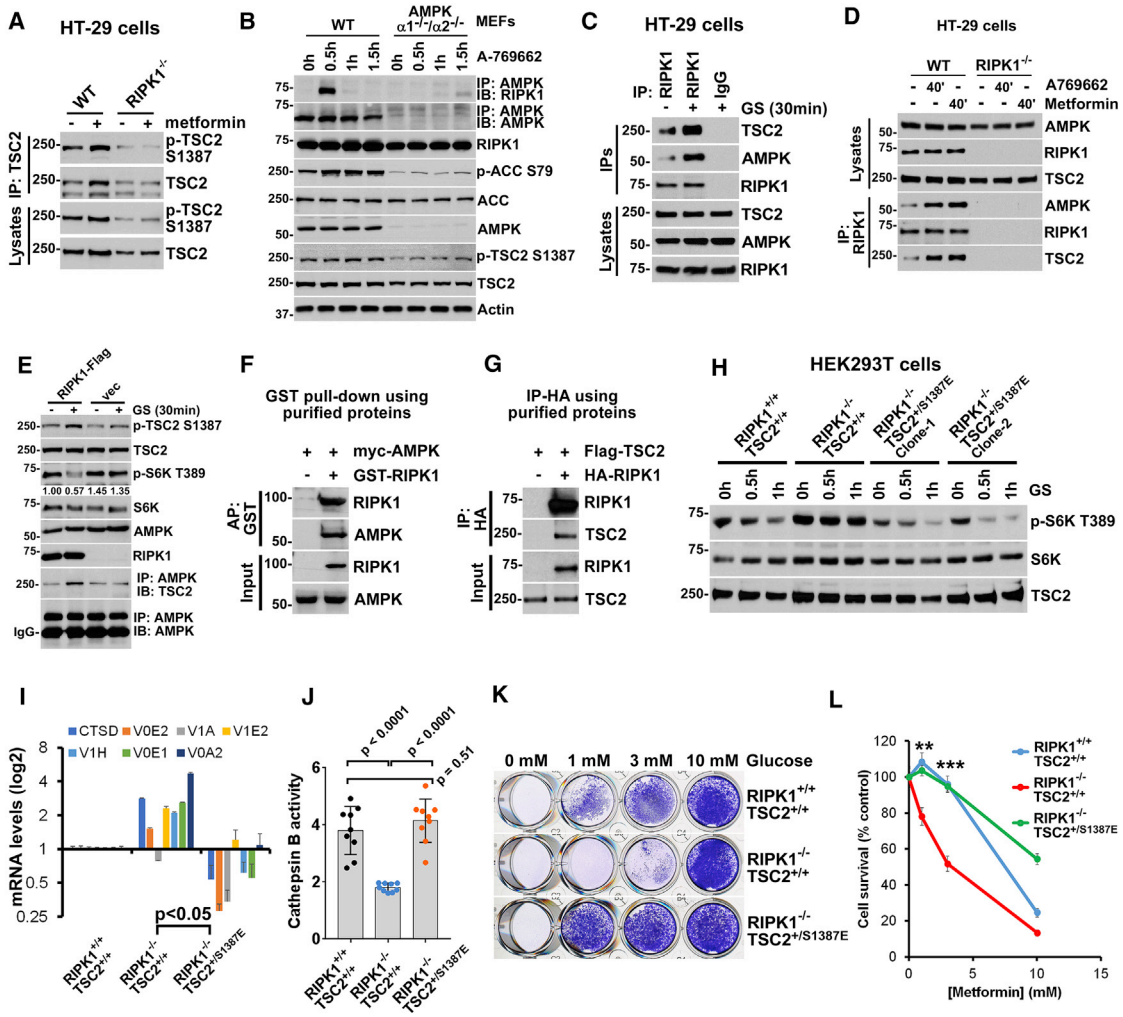

Figure 4. RIPK1 Promotes AMPK-TSC2 Interaction and mTORC1 Inhibition

(A) Induction of phosphorylation of the AMPK site Ser1387 in TSC2 is compromised upon RIPK1 loss. Cells were treated with 5 mM metformin for 1 h, and endogenous TSC2 was immunoprecipitated.

(B) Endogenous AMPK and RIPK1 interact upon AMPK activation by A-769662. AMPK$\alpha1^{-/-}/\alpha2^{-/-}$ MEF cells were used as a negative control.

(C) Endogenous RIPK1, AMPK, and TSC2 interact upon glucose starvation (GS). Cells were glucose starved, and endogenous RIPK1 was immunoprecipitated (IPs). Lysates and immunoprecipitated proteins were immunoblotted with indicated antibodies. TrueBlot secondary antibodies were used for immunoblotting of the IPs.

(D) Endogenous RIPK1, AMPK, and TSC2 interact upon AMPK activation. Cells were treated with 100 μM A-769662 or 5 mM metformin for 40 min, and endogenous RIPK1 was immunoprecipitated. Cell lysates and immunoprecipitated proteins were immunoblotted with indicated antibodies. RIPK1$^{-/-}$ cells were used as negative control. TrueBlot secondary antibodies were used for immunoblotting of the IPs.

(E) Endogenous AMPK-TSC2 interaction is compromised upon RIPK1 loss. Indicated cells were subjected to GS, and AMPK was immunoprecipitated. The values under the p-S6K panel indicate p-S6K/S6K quantification of the bands with respect to the first lane.

(F) Purified RIPK1 and AMPK interact directly. GST-RIPK1 and MYC-AMPK were expressed and purified from HEK293T RIPK1$^{-/-}$ cells (separately) and combined for a GST pull-down.

(G) Purified RIPK1 and TSC2 interact directly. Indicated proteins were purified as in (E) and combined for IP-HA.

(H) TSC2^{S1387E} knock-in rescues the compromised mTORC1 inhibition upon GS.

(I) TSC2^{S1387E} knock-in rescues the aberrant lysosomal gene expression levels of RIPK1$^{-/-}$ HEK293T cells.

(J) TSC2^{S1387E} knock-in rescues defective lysosomal activity of RIPK1$^{-/-}$ HEK293T cells.

(K) TSC2^{S1387E} knock-in rescues defective survival in low glucose conditions, as determined by crystal violet staining.

(L) As in (J), except metformin was used instead of GS.

*p < 0.05, **p < 0.01, ***p < 0.001. Mean and SEM are plotted.

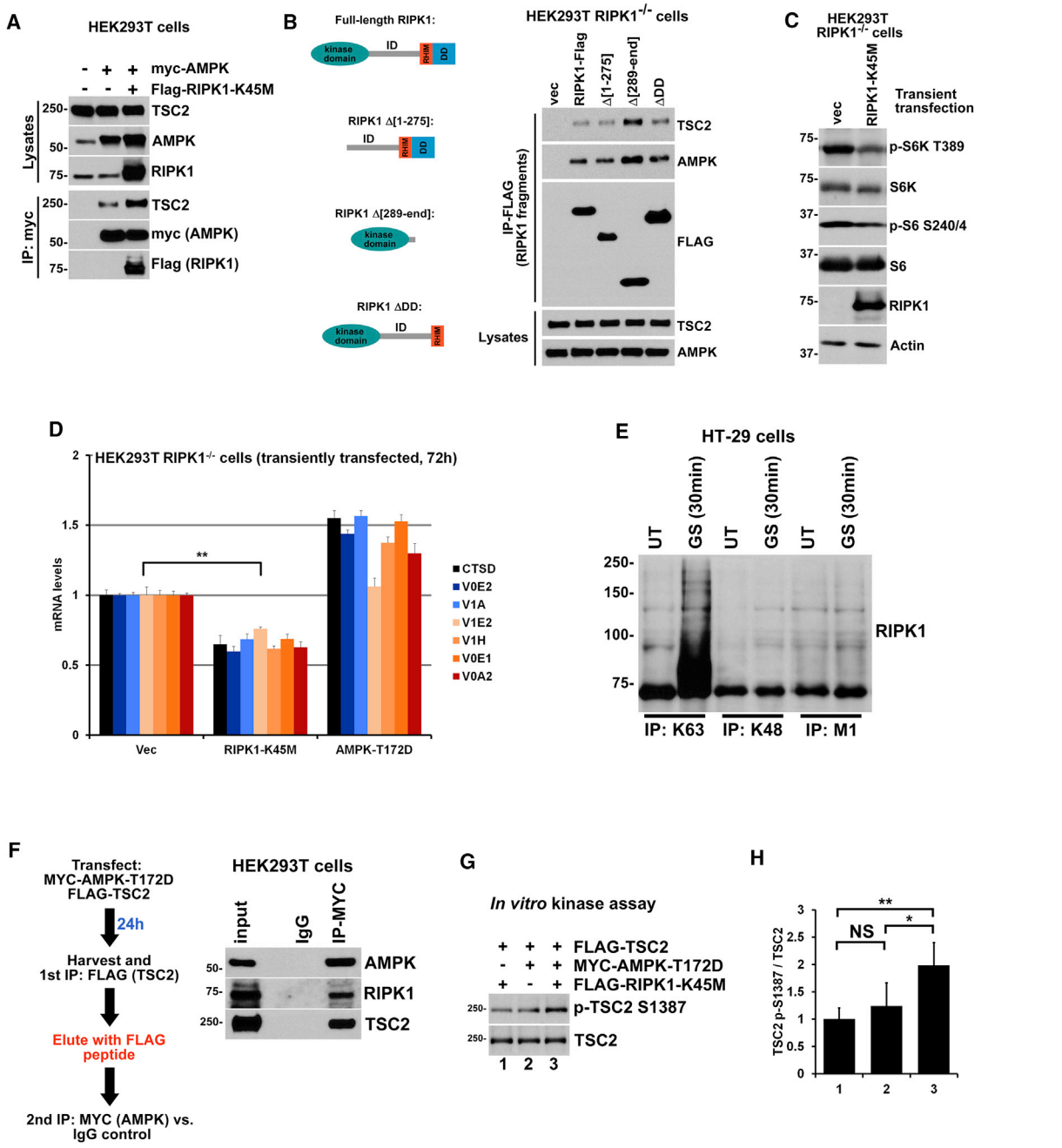

Figure 5. RIPK1 Scaffold Function Promotes AMPK-TSC2 Interaction

(A) Transfected MYC-AMPK^{T172D} and FLAG-RIPK1^{K45M}, as well as endogenous TSC2, interact in cell lysates. HEK293T cells were transfected with the indicated plasmids, and 48 h later, cell lysates were subjected to anti-MYC immunoprecipitation. Cell lysates and immunoprecipitated proteins were immunoblotted with indicated antibodies. Note that the amount of endogenous TSC2 co-immunoprecipitated with AMPK increases in the third lane, where RIPK1^{K45M} was transfected. TrueBlot secondary antibodies were used for immunoblotting of the IPs.

(B) The region between the RIPK1 kinase domain and intermediate domain (ID) is sufficient for RIPK1-AMPK/TSC2 interaction. Indicated fragments of FLAG-RIPK1 were expressed in HEK293T RIPK1$^{-/-}$ cells, and cell lysates were subjected to anti-FLAG immunoprecipitation. Cell lysates and immunoprecipitated proteins were immunoblotted with indicated antibodies. The diagram indicates the domains of the RIPK1 remaining in each construct employed. TrueBlot secondary antibodies were used for immunoblotting of the IPs.

(C) Overexpression of kinase-dead RIPK1^{K45M} inhibits mTORC1 signaling. HEK293T RIPK1$^{-/-}$ cells were transfected as indicated for 24 h, and cell lysates were immunoblotted with indicated antibodies.

(D) Rescue of the elevated lysosomal gene expression in RIPK1$^{-/-}$ HEK293T cells. Both wild-type and kinase-dead (K45M) RIPK1 can rescue the elevated levels of lysosomal genes.

(legend continued on next page)

Please cite this article in press as: Najafov et al., RIPK1 Promotes Energy Sensing by the mTORC1 Pathway, Molecular Cell (2020), https://doi.org/10.1016/j.molcel.2020.11.008

increase in lysosomal biogenesis and consistent with the finding that RIPK1 loss results in defective lysosomes in the tissues (Figures 6A–6C).

Furthermore, RIPK3 and CASP8 levels were significantly elevated in the large intestines of the neonatal RIPK1$^{-/-}$ mice (Figure 6A). We also found that MLKL phosphorylation at Ser345 (the RIPK3 phosphorylation site) was induced in RIPK1$^{-/-}$ large intestines, consistent with the reported partial rescue from RIPK1$^{-/-}$ lethality by *Mlkl* or *Ripk3* knockout (Dillon et al., 2014; Kaiser et al., 2014; Rickard et al., 2014; Silke et al., 2015) and the accumulation of RIPK3 seen in the RIPK1$^{-/-}$ tissues (Figure 6A). Compared to intestines, the differences in RIPK3 levels were less pronounced between wild-type and RIPK1$^{-/-}$ neonatal liver, lungs, and heart tissues and minimal or no changes were found in the brain tissue (Figure S7B).

Wild-type neonates displayed no signs of starvation, as judged by low levels of AMPK activation indicated by the lack of p-ACC (Figure 6A), which is consistent with the effect of *de novo* glucose generation from the amino acids produced via neonatal autophagy (Efeyan et al., 2013). On the other hand, RIPK1$^{-/-}$ neonates showed high levels of starvation, as judged by dramatically elevated AMPK activation levels (Figure 6A, see p-ACC levels), which is consistent with the low blood glucose levels previously observed in these mice at the neonatal stage (Rickard et al., 2014). However, unlike phosphorylation of the AMPK target ACC, the phosphorylation of TSC2 Ser1387 (the AMPK target site) was not detected in the large intestines of RIPK1$^{-/-}$ mice, whereas mTORC1 activation levels were strongly elevated despite the high levels of AMPK activation (Figure 6A).

This is in accord with our mechanistic findings that RIPK1 is required for the suppression of mTORC1 activity downstream of AMPK via TSC2 phosphorylation at Ser1387 (Figure 3). Additionally, we found no elevated mTORC1 activity, MLKL phosphorylation induction, or accumulation of RIPK3/CASP8 in the large intestines of neonatal RIPK1$^{+/-}$ heterozygous mice, consistent with the lack of lethality in these mice (Figure 6E).

Remarkably, injecting pregnant RIPK1$^{+/-}$ heterozygous mice with mTORC1 inhibitor rapamycin prolonged the survival of the RIPK1$^{-/-}$ neonates from 3 to 6 days (Figure 6F), which is a more significant protection from neonatal lethality in the context of previously reported protection levels for RagA$^{GTP/GTP}$ mice, potentially because we injected rapamycin at E20 stage, whereas Efeyan et al. (Efeyan et al., 2013) performed subcutaneous injections of the RagA$^{GTP/GTP}$ neonatal pups. This result is also consistent with our findings that RIPK1 loss results in failure to inhibit mTORC1 (Figure 6A) and that mTORC1-driven dysregulation of lysosomal homeostasis can be rescued by rapamycin treatment (Figures 1F–1H and S1D S1I), as well as with the Efeyan et al. study's showing that elevated mTORC1 activity results in neonatal lethality (Efeyan et al., 2013).

RIPK1 Loss and Lysosomal Inhibition Promote RIPK3/CASP8 Accumulation and Cell Death

Using the protein synthesis inhibitor cycloheximide chase experiments, we confirmed that compromised degradation of p62, RIPK3, and CASP8 indeed occurred upon loss of RIPK1 (Figure 7A). We found that RIPK1$^{-/-}$ HT-29 cells were sensitized to cell death induced by TNFα + zVAD.fmk combination following 48 h of the treatment (Figure 7B). Consistently, this treatment induced MLKL and RIPK3 phosphorylation at much later time points (16–24 h) (Figure S7D) than canonical necroptosis signaling (4–6 h) (Najafov et al., 2019). Interestingly, this cell death effect was not seen in MEFs, suggesting a cell type-specific nature (Figure 7C). We confirmed that the lack of necessity for a Smac mimetic co-treatment in the TNFα + zVAD (TZ)-induced cell death of RIPK1$^{-/-}$ HT-29 cells was not due to a potential loss of IAP protein expression (Figure S7E). Importantly, in accord with our model, this sensitivity, but not the canonical necroptosis signaling in wild-type HT-29 cells, was reduced by a 16 h pre-treatment with Torin-1 (Figure 7D), and the increased levels of RIPK3 and CASP8 were also rescued by this treatment (Figure 7E). Notably, loss of autophagy via Atg5 knockout did not have the same effect on necroptosis sensitivity (Figure S7F).

Interestingly, in agreement with the notion that lysosomal defects promote RIPK3/CASP8 accumulation and cell death, prolonged (72 h) inhibition of lysosomes by the anti-malarial drug chloroquine (CQ) resulted in a RIPK3/CASP8-mediated cell death of wild-type cells (Figures 7F–7H), and this effect was enhanced by RIPK1 loss (Figures 7I and 7J). Additionally, lysosomal inhibition by either CQ or E64D/Pepstatin combination sensitized cells to (TZ)-induced cell death (Figures 7K–7M). Finally, in RIPK1$^{-/-}$ MEFs, RIPK3 accumulated in puncta that were both cytosolic and lysosomal (Figure 7N), consistent with our data showing its accumulation and lack of degradation due to defective lysosomal homeostasis in RIPK1$^{-/-}$ cells.

These findings further confirm that RIPK1 promotes lysosomal homeostasis, which is critical for degradation of RIPK3 and CASP8 to ensure their physiological levels. Upon loss of RIPK1 and consequently dysregulated lysosomal homeostasis, or upon pharmacological inhibition of lysosomes, RIPK3 and CASP8 accumulate beyond physiological levels, which sensitizes cells to apoptosis and necroptosis, in agreement with previous studies (Christofferson et al., 2014; Kelliher et al., 1998; Silke et al., 2015).

(E) RIPK1 is ubiquitinated via K63-linked ubiquitin chains following glucose starvation (GS). HT-29 cells were glucose starved for 30 min, cells were lyzed in a 6 M urea buffer, and lysates were subjected to immunoprecipitation via indicated ubiquitin chain-specific nanobodies. Immunoprecipitated proteins were immunoblotted for endogenous RIPK1. TrueBlot secondary antibodies were used for immunoblotting of the IPs.

(F) RIPK1, AMPK, and TSC2 form a ternary complex. HEK293T cells were co-transfected with MYC-AMPK^{T172D} and FLAG-TSC2 for 48 h. Cell lysates were subjected to anti-FLAG immunoprecipitation; the proteins were eluted with FLAG peptide and subjected to anti-MYC immunoprecipitation. Cell lysates and immunoprecipitated proteins were immunoblotted with indicated antibodies. TrueBlot secondary antibodies were used for immunoblotting of the IPs.

(G) Kinase-dead RIPK1^{K45M} promotes TSC2 phosphorylation by AMPK^{T172D} at Ser1387 in an *in vitro* kinase assay. Proteins were purified separately from RIPK1$^{-/-}$ HEK293T cells. Kinase reaction was carried out for 30 min at 30°C.

(H) The p-TSC2 S1387 band intensities from (B) were quantified and normalized to total TSC2 levels. The experiment was repeated in triplicates. *$p < 0.05$, **$p < 0.01$.

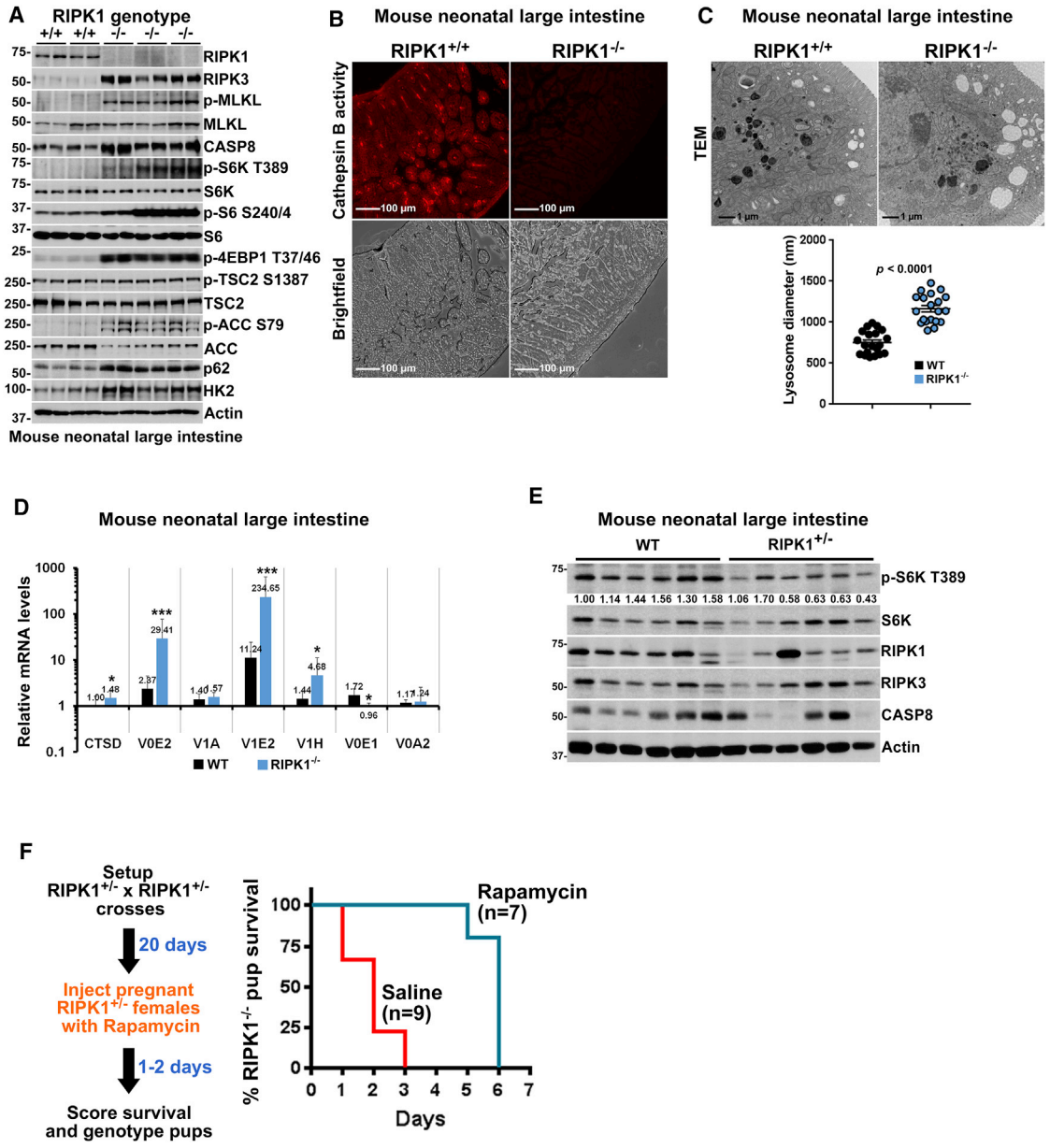

Figure 6. RIPK1 Loss Results in Lysosomal Dysfunction in Neonatal Mice

(A) RIPK1 knockout results in the accumulation of RIPK3 and CASP8, as well as other lysosomal targets—HK2, CTSD, and p62—in the large intestine tissues of neonatal mice, while mTORC1 pathway is overactive, despite high levels of AMPK activation. Samples were loaded in duplicates per animal.

(B) RIPK1 knockout results in defective lysosomal activity in the large intestine tissues of neonatal mice, as determined by cathepsin B probe Magic Red.

(C) Lysosomal enlargement in RIPK1$^{-/-}$ large intestinal villi epithelial cells, as determined by transmission electron microscopy (TEM). Inset: quantification of the lysosomal diameter levels is shown (n = 60). Student's t test was employed. Error bars: SEM.

(D) Lysosomal gene expression dysregulation in RIPK1$^{-/-}$ large intestine tissues.

(E) RIPK1$^{+/-}$ neonatal large intestine tissues do not show mTORC1 pathway overactivation or the RIPK3/CASP8 accumulation seen in RIPK1$^{-/-}$ tissues. Tissue lysates were immunoblotted with indicated antibodies. The values under the p-S6K panel indicate p-S6K/S6K quantification of the bands with respect to the first lane.

(F) mTORC1 inhibition promotes survival of RIPK1$^{-/-}$ mice. Pregnant RIPK1$^{+/-}$ mice were given rapamycin via one intraperitoneal injection. Pups were left with the mother, and their survival was monitored. Pups were genotyped post-mortem.

*p < 0.05, **p < 0.01, ***p < 0.001. Mean and SEM are plotted.

Please cite this article in press as: Najafov et al., RIPK1 Promotes Energy Sensing by the mTORC1 Pathway, Molecular Cell (2020), https://doi.org/10.1016/j.molcel.2020.11.008

CellPress

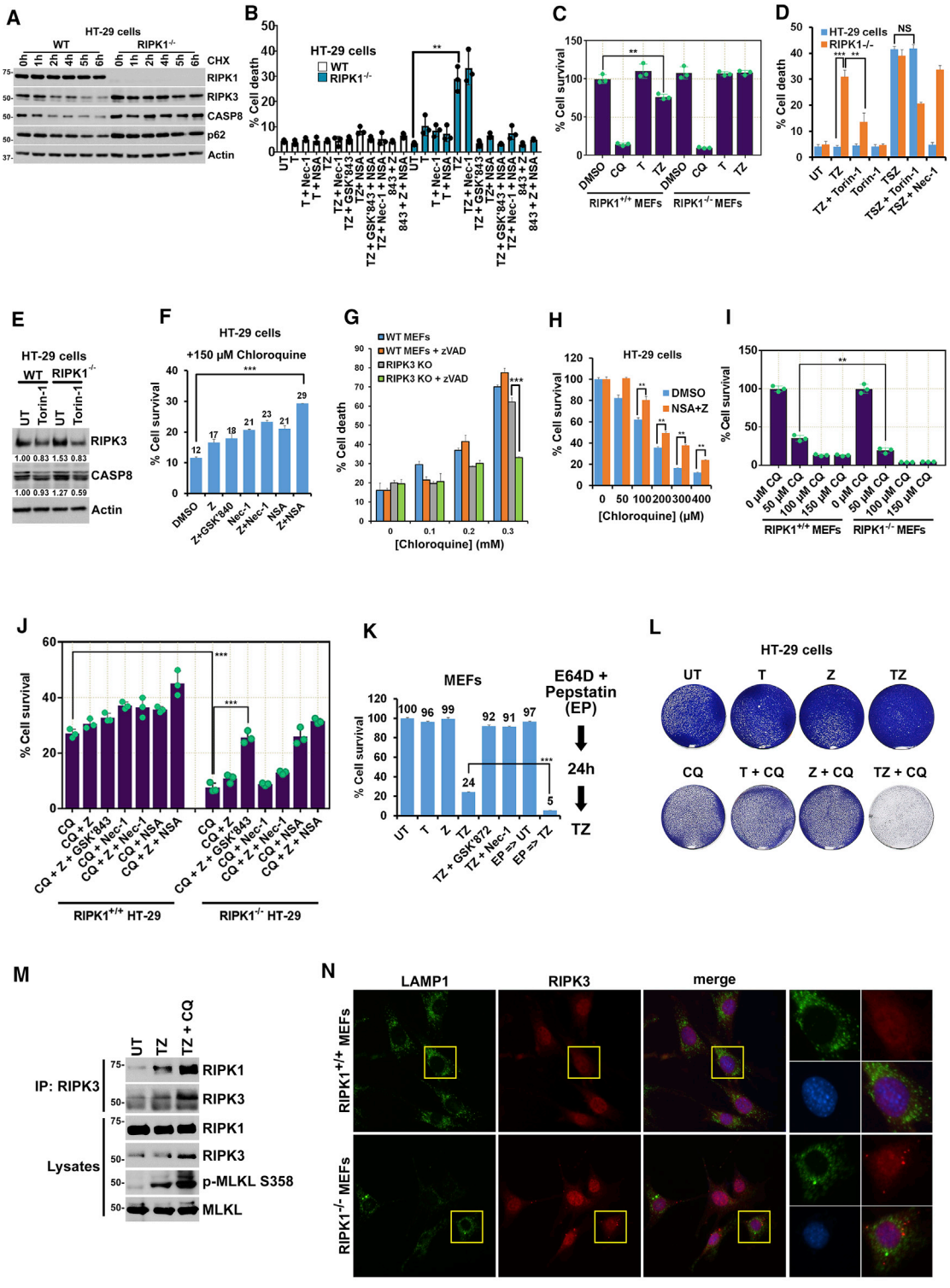

Figure 7. RIPK1 Loss and Lysosomal Defects Sensitize to Necroptosis

(A) Lysosomal degradation of RIPK3 and CASP8 is compromised in RIPK1$^{-/-}$ HT-29 cells. Cells were treated with protein synthesis inhibitor cycloheximide (CHX) at 20 μg/mL dose for the indicated time points, and cell lysates were immunoblotted with indicated antibodies.

(B) RIPK1$^{-/-}$ HT-29 cells are sensitized to cell death induced by TNFα + zVAD.fmk (TZ) combination. Cells were treated with 50 ng/mL hTNFα + 30 μM zVAD.fmk for 48 h. Cell death was assessed by Toxilight reagent.

(legend continued on next page)

Please cite this article in press as: Najafov et al., RIPK1 Promotes Energy Sensing by the mTORC1 Pathway, Molecular Cell (2020), https://doi.org/10.1016/j.molcel.2020.11.008

DISCUSSION

It is noteworthy to mention that our study sheds light on a potential mechanism of action for the diabetes drug metformin and other AMPK activating drugs in the context of the inhibition of the mTORC1 pathway downstream of RIPK1, as well as lysosomal homeostasis. Our findings also align with the recent report showing that AMPK promotes lysosomal gene expression during glucose starvation (Eichner et al., 2019), placing RIPK1 as a key mediator of this process downstream of AMPK and upstream of the TSC2-mTORC1 pathway. The components of the signaling pathway that recruit TSC2 to the RIPK1-AMPK complex remain to be determined. Importantly, our findings are in complete accord with the previously reported increase in sensitivity of TSC2$^{-/-}$ cells to glucose starvation (Inoki et al., 2003).

Previously, Rag GTPases have been shown to be critical for neonatal glucose sensing (Efeyan et al., 2013). RIPK1$^{-/-}$ cells displayed no defect in Rag-mediated mTORC1 activation, as the localization of mTORC1 to lysosomes and inhibition of mTORC1 upon amino acid starvation was not impaired. Thus, although Rags constitute the lysosome-vATPase-Rag-mTORC1 axis of the glucose sensing upstream of mTORC1 (Efeyan et al., 2013), the RIPK1-mediated TSC2 phosphorylation by AMPK in the TSC2-Rheb-mTORC1 (Huang and Manning, 2008) axis also contributes to sensing cellular glucose/energy levels. This, in turn, helps to control cell metabolism by coordinating the growth factor-TSC2-mediated input into the mTORC1 pathway with the availability of energy resources.

Moreover, recent studies have shown that, in addition to TSC2 and Raptor, AMPK also impinges into the mTORC1 pathway via the aldolase-v-ATPase-Ragulator pathway (Hardie and Lin, 2017; Lin and Hardie, 2018; Zhang et al., 2017; Zong et al., 2019). Our data indicate that the amino acid sensing capacity (Figures 3B and 3C), as well as mTOR localization (Figure S2), is not affected in RIPK1$^{-/-}$ cells, suggesting that RIPK1 does not impinge on mTORC1 via the Ragulator pathway. Furthermore, our TSC2 S1387E knockin data (Figures 4G–4K and S6A–S6C) suggests that the only compromised component of the mTORC1 pathway in RIPK1-deficient cells is the AMPK-TSC2 interaction and the phosphorylation of the latter at S1387.

Recently, mTORC1 overactivation due to TSC1 loss has been shown to lead to T cell loss, whereas on the other hand, RIPK1/RIPK3/CASP8 triple knockout mice (which are expected to also have mTORC1 overactivation due to loss of RIPK1) display T cell expansion and develop lymphoproliferative disease (LPR), which is a model of the human autoimmune lymphoproliferative syndrome (ALPS) (Teachey et al., 2006; Tummers et al., 2020; Yang et al., 2011). While future studies will shed light on the exact mechanisms of this difference in phenotypes, one can speculate that the difference between these two outcomes of mTORC1 overactivation could be because RIPK1 does not play a role in AMPK-independent regulation of mTORC1, whereas the TSC complex, in which TSC1 plays a role, integrates not only AMPK but also growth factor signaling and other cues that control mTORC1 (Huang and Manning, 2008). Additionally, the lack of CASP8/RIPK3 in the RIPK1/RIPK3/CASP8 triple knockout mice could be limiting T cell death, allowing mTORC1 overactivation-driven cell growth to drive the T cell expansion seen in LPR/ALPS.

Similarly, although TSC2 loss results in benign tumors in multiple tissues (heart, lungs, liver, kidneys, eyes, and skin) as well as neuronal phenotypes, to our knowledge, loss of RIPK1 does not result in tumors (Huang and Manning, 2008; Rickard et al., 2014). The key difference between the RIPK1-deficient and TSC2-deficient contexts, once again, could be the ability of TSC to integrate signals from other kinases (e.g., Akt, RSK, ERK, and GSK3) in RIPK1 null settings but not in TSC2 null settings (Huang and Manning, 2008).

Interestingly, the dysregulation of the mTORC1 activity levels, lysosomal gene expression dysregulation, and RIPK3 accumulation in the RIPK1$^{-/-}$ neonates were detected in a tissue-specific

(C) Wild-type or RIPK1$^{-/-}$ MEFs were treated with 150 μM Chloroquine (CQ), 50 ng/mL TNFα, or TNFα + 30 μM zVAD for 24 h. Cells were fixed and stained with crystal violet to measure cell viability.
(D) The sensitivity of RIPK1$^{-/-}$ HT-29 cells to TZ (but not to canonical necroptosis signaling in wild-type HT-29 cells) can be rescued by Torin-1. Cells were treated as in (B), except cells were pre-treated with 0.25 μM Torin-1 for 16 h and Torin-1 was washed out. SM-164 (S) was used at 100 nM. Cell death was assessed by SYTOX Green reagent after 48 h of treatment.
(E) Elevated RIPK3 and CASP8 levels in RIPK1$^{-/-}$ cells can be rescued by mTORC1 inhibition by Torin-1. HT-29 cells were treated for 16 h with 0.25 μM Torin-1, and cell lysates were immunoblotted with indicated antibodies. The values under the panels indicate the quantification of the bands normalized to actin with respect to the first lanes.
(F) Lysosomal inhibition for 72 h by CQ at 150 μM drives RIPK3/CASP8-mediated cell death in HT-29 cells that can be blocked by inhibition of MLKL (using NSA) and pan-caspase inhibitor zVAD (Z). Cell death was determined with CellTiterGlo assay. RIPK1 inhibitor Nec-1, RIPK3 inhibitor GSK′840, and MLKL inhibitor NSA were used at 20 μM, 10 μM, and 1 μM, respectively.
(G) Lysosomal inhibition by CQ at indicated doses for 72 h drives RIPK3/CASP8-mediated cell death in MEFs that can only be potently blocked by combined knockout of RIPK3 and pan-caspase inhibitor zVAD (Z). Cell death was determined with Toxilight assay.
(H) Dose-dependent cell death induced by CQ in HT-29 cells at 72 h. MLKL inhibitor NSA and pan-caspase inhibitor zVAD (Z) were used at 1 μM and 30 μM, respectively.
(I) Wild-type or RIPK1$^{-/-}$ MEFs were treated with indicated concentrations of CQ for 24 h. Cells were fixed and stained with crystal violet to measure cell viability.
(J) Wild-type or RIPK1$^{-/-}$ HT-29 cells were treated with 150 μM of CQ in the presence of indicated compounds for 24 h. Cells were fixed and stained with crystal violet to measure cell viability. Z: 20 μM zVAD.fmk; GSK′843: RIPK3 inhibitor, 10 μM; Nec-1: RIPK1 inhibitor, 10 μM; NSA: MLKL inhibitor, 1 μM.
(K) Lysosomal inhibition by E64D/Pepstatin (EP) combination sensitizes wild-type MEFs to TZ-induced necroptosis. Cells were pre-treated with EP for 24 h and stimulated with TZ for 16 h. E64D, Pepstatin, RIPK1 inhibitor Nec-1, RIPK3 inhibitor GSK′840, and MLKL inhibitor NSA were used at 10 μg/mL, 10 μg/mL, 20 μM, 10 μM, and 1 μM, respectively.
(L) As in (E), except HT-29 cells and CQ were used, and crystal violet assay was employed to assess cell survival.
(M) Lysosomal inhibitor CQ sensitizes HT-29 cells to TZ-induced RIPK1-RIPK3 necrosome formation and MLKL phosphorylation. HT-29 cells were treated with 150 μM CQ for 24 h followed by 4 h TZ treatment.
(N) RIPK3 accumulation in RIPK1$^{-/-}$ MEFs, as determined by immunofluorescence.

Please cite this article in press as: Najafov et al., RIPK1 Promotes Energy Sensing by the mTORC1 Pathway, Molecular Cell (2020), https://doi.org/10.1016/j.molcel.2020.11.008

manner with the most pronounced changes found in the organs most exposed to the environment (intestines and lungs) and the least pronounced changes found in organs shielded from it (brain and heart) (Figures 6A and S7A–S7C). Whether neonatal exposure to pathogens and activation of the pathogen-responsive pathways, such as Toll-like receptor signaling, play a role in this effect, remains to be elucidated. However, it is also possible that the aforementioned tissue-specific differences are due to differences in the neonatal autophagy induction (Kuma et al., 2004).

These observations suggest that the neonatal lethality induced by RIPK1 loss could be, at least partially, due to a defect in a lysosomal degradation pathway that leads to the accumulation of RIPK3 and CASP8, thus, sensitizing the neonatal cells to a cell death pathway driven by these molecules. Atg5 has been linked to cell death (Martinez et al., 2016). To assess the mechanistic similarity between the neonatal lethality of RIPK1$^{-/-}$ and Atg5$^{-/-}$ mice, we attempted to rescue the lethality of Atg5$^{-/-}$ mice by crossing them into RIPK3$^{-/-}$ and RIPK3$^{-/-}$;FADD$^{-/-}$ backgrounds. Our data show that neither loss of RIPK3 (Table S1) nor loss of RIPK3 and FADD can protect the lethality of Atg5$^{-/-}$ (Table S2). Thus, unlike in RIPK1$^{-/-}$ mice, the lethality of which can be rescued by RIPK3$^{-/-}$;FADD$^{-/-}$ double knockout (Dillon et al., 2014), the lethality of Atg5$^{-/-}$ mice is likely to involve different or additional mechanisms.

Our results indicate that lysosomes are important negative regulators of RIPK3/CASP8-driven cell death (Figure 7). Moreover, our study links mTORC1, a nutrient sensing complex that is overactivated in the majority of cancers, to the regulation of apoptosis and necroptosis via RIPK3/CASP8 degradation. Thus, it will be important to understand how the overactivation of mTORC1 in cancer impacts the regulation of cancer cell sensitivity to apoptosis and necroptosis.

We consistently see increased expression of various (but not all) v-ATPase subunits upon RIPK1 loss (Figures 1, 6, S1G–S1I, S7A, and S7C). It is noteworthy that a lack of the v-ATPase subunit balance induced by either haploinsufficiency (Rizzo et al., 2007) or overexpression of the subunits has been previously demonstrated to be deleterious to the pump function (Guida et al., 2018; Papp et al., 2003; Petzoldt et al., 2013). The ATP6V1E2 subunit is the most dysregulated out of the v-ATPase subunits that we have analyzed (Figures 1F, 6D, S1H, and S7A). In agreement with these reports, we found that even transient (48 h) ectopic overexpression of the ATP6V1E2 subunit by itself can cause lysosomal dysfunction (Figures S7G and S7H). Together, our data and the aforementioned studies indicate that the v-ATPase pump is sensitive to the subunit expression imbalance and suggest that the lysosomal defect in RIPK1$^{-/-}$ cells could be due to such imbalance that the non-stoichiometric overexpression of the subunits introduces; ATP6V1E2 overexpression is a potential driver of the imbalance and pump misassembly. The exact transcriptional mechanism of such dysregulated expression of the v-ATPase subunits in RIPK1$^{-/-}$ cells, which also could be due to a compensatory effect, remains to be elucidated.

Unlike AMPK null cells, which have defective and minimally expressed lysosomal genes (Eichner et al., 2019; Young et al., 2016), RIPK1 null cells appear to be defective in the same machinery as TSC2 null cells since both RIPK1 and TSC2 loss results in a dysregulation, rather than a downregulation, of v-ATPase gene expression, which is consistent with our model stating that RIPK1 promotes TSC2 regulation by AMPK.

It is worth mentioning that although LC3 lipidation and degradation could be useful in many biological settings, we did not employ this marker of autophagy and lysosomal degradation because, in RIPK1-deficient cells, mTORC1 activity is elevated, which would result in suppressed LC3 lipidation (i.e., decreased autophagy induction), and at the same time, lysosomes are defective, which would result in accumulation of LC3-II. Instead, we used lysosomal substrates p62, RIPK1, RIPK3, and CASP8, which are known to be degraded by lysosomes and are directly relevant to the study, unlike LC3 lipidation itself.

Our study also sheds light on the mechanism of disorders such as primary immunodeficiency and inflammatory bowel disorders, which were recently linked to biallelic deletions of RIPK1 (Cuchet-Lourenço et al., 2018; Li et al., 2019), and places mTOR inhibition as a putative treatment for such disorders since rapamycin can rescue phenotypes induced by RIPK1 loss (Figures 1, S1, and S6D). Moreover, since RIPK1-deficient cells are more sensitive to metformin and glucose starvation, our work suggests that low RIPK1 expression is a potential biomarker for metformin sensitivity of tumors and, thus, cancer therapies that involve metformin or other types of agents that induce AMPK activation could benefit from targeting RIPK1^{low} tumors.

In summary, our study identifies an unexpected, kinase activity-independent role for RIPK1 as a mediator of the AMPK/TSC2-driven cellular sensing of the energy levels that impinge on the mTORC1 pathway, positioning RIPK1 as a key regulator of anabolism/catabolism and lysosomal homeostasis and, therefore, the capability to conduct autophagy (Figure S7I). Further studies are required in order to determine how this role of RIPK1 fits with its role in promoting neonatal survival. Thus, in addition to its pro-survival function as a promoter of the NF-κB pathway, the scaffold function of RIPK1 plays an important role in promoting energy sensing by the AMPK-TSC2-mTORC1 pathway by functioning as an indirect inhibitor of the RIPK3/CASP8-driven cell death pathways.

Limitations

While our data indicate that the lysosomal dysfunction in RIPK1-deficient cells is due to the elevated mTORC1 activity and transcriptional dysregulation that can be rescued by rapamycin and Torin-1, further studies are required to define the transcriptional mechanisms that mediate this dysregulation downstream of mTORC1. The cell and tissue specificity of (1) mTORC1 regulation by the RIPK1-AMPK-TSC2 signaling and (2) sensitization of cells to cell death following accumulation of RIPK3/CASP8 due to lysosomal dysfunction in RIPK1-deficient cells has not been fully defined in this study. Because of inhibition of autophagy by high mTORC1 activity levels (through ULK1) in RIPK1-deficient cells and a concurrent lysosomal activity defect (through lysosomal gene expression dysregulation), autophagy flux experiments are incompatible with RIPK1-deficient cells to study autophagy or lysosomal function. The mechanism of action of RIPK1 in mediating TSC2 phosphorylation by AMPK and whether additional proteins are part of this process remains to be determined.

Please cite this article in press as: Najafov et al., RIPK1 Promotes Energy Sensing by the mTORC1 Pathway, Molecular Cell (2020), https://doi.org/10.1016/j.molcel.2020.11.008

STAR★METHODS

Detailed methods are provided in the online version of this paper and include the following:

- KEY RESOURCES TABLE
- RESOURCE AVAILABILITY
  - Lead Contact
  - Materials Availability
  - Data and Code Availability
- EXPERIMENTAL MODEL AND SUBJECT DETAILS
  - Cell lines
  - Animal work
- METHOD DETAILS
  - Materials
  - Molecular Cloning, Plasmids and qRT-PCR
  - Generation of RIPK1 knockout and TSC2 S1387E knock-in cell lines using CRISPR/cas9
  - Glucose starvation treatments
  - Cell Lysis, Immunoprecipitation, and Immunoblotting
  - Protein purification and *in vitro* kinase assays
  - Ubiquitin chain immunoprecipitation
  - Light Microscopy
  - Electron Microscopy and Lysosomal Size Measurements
  - Cell growth and cell death assays
  - pHrodo staining and flow cytometry
  - Cathepsin B Activity
- QUANTIFICATION AND STATISTICAL ANALYSIS

SUPPLEMENTAL INFORMATION

Supplemental Information can be found online at https://doi.org/10.1016/j.molcel.2020.11.008.

ACKNOWLEDGMENTS

This work was supported in part by the Ludwig Cancer Center at Harvard Medical School. We thank the Nikon Imaging Center at Harvard Medical School for assistance with microscopy. We are grateful to Dr. Vishva Dixit for RIPK3 knockout mice, Dr. Douglas R. Green for FADD knockout mice, Dr. Michelle Kelliher for RIPK1 knockout mice, Dr. Benoit Viollet for AMPK knockout MEFs, and Dr. Gerta Hoxhaj for TSC2 knockout MEF lysates.

AUTHOR CONTRIBUTIONS

A.N. and J.Y. conceived the project, designed the experiments, analyzed the data, and wrote the manuscript. A.N. performed most of the experiments. H.S.L., A.K.M., P.A., L.M., H.X., and A.O. performed and assisted with experiments. H.S.L. and L.M. assisted with the manuscript. H.W. provided samples or reagents.

DECLARATION OF INTERESTS

Junying Yuan is a consultant for Denali Therapeutics and Sanofi S.A.

Received: April 14, 2020
Revised: August 31, 2020
Accepted: November 4, 2020
Published: December 2, 2020

REFERENCES

Arslan, S.Ç., and Scheidereit, C. (2011). The prevalence of TNFα-induced necrosis over apoptosis is determined by TAK1-RIP1 interplay. PLoS ONE *6*, e26069.

Christofferson, D.E., Li, Y., and Yuan, J. (2014). Control of life-or-death decisions by RIP1 kinase. Annu. Rev. Physiol. *76*, 129–150.

Cool, B., Zinker, B., Chiou, W., Kifle, L., Cao, N., Perham, M., Dickinson, R., Adler, A., Gagne, G., Iyengar, R., et al. (2006). Identification and characterization of a small molecule AMPK activator that treats key components of type 2 diabetes and the metabolic syndrome. Cell Metab. *3*, 403–416.

Cuchet-Lourenço, D., Eletto, D., Wu, C., Plagnol, V., Papapietro, O., Curtis, J., Ceron-Gutierrez, L., Bacon, C.M., Hackett, S., Alsaleem, B., et al. (2018). Biallelic *RIPK1* mutations in humans cause severe immunodeficiency, arthritis, and intestinal inflammation. Science *361*, 810–813.

Dannappel, M., Vlantis, K., Kumari, S., Polykratis, A., Kim, C., Wachsmuth, L., Eftychi, C., Lin, J., Corona, T., Hermance, N., et al. (2014). RIPK1 maintains epithelial homeostasis by inhibiting apoptosis and necroptosis. Nature *513*, 90–94.

de Almagro, M.C., Goncharov, T., Newton, K., and Vucic, D. (2015). Cellular IAP proteins and LUBAC differentially regulate necrosome-associated RIP1 ubiquitination. Cell Death Dis. *6*, e1800.

Dikic, I., and Elazar, Z. (2018). Mechanism and medical implications of mammalian autophagy. Nat. Rev. Mol. Cell Biol. *19*, 349–364.

Dillon, C.P., Weinlich, R., Rodriguez, D.A., Cripps, J.G., Quarato, G., Gurung, P., Verbist, K.C., Brewer, T.L., Llambi, F., Gong, Y.-N., et al. (2014). RIPK1 blocks early postnatal lethality mediated by caspase-8 and RIPK3. Cell *157*, 1189–1202.

Dondelinger, Y., Jouan-Lanhouet, S., Divert, T., Theatre, E., Bertin, J., Gough, P.J., Giansanti, P., Heck, A.J.R., Dejardin, E., Vandenabeele, P., and Bertrand, M.J. (2015). NF-κB-Independent Role of IKKα/IKKβ in Preventing RIPK1 Kinase-Dependent Apoptotic and Necroptotic Cell Death during TNF Signaling. Mol. Cell *60*, 63–76.

Efeyan, A., Zoncu, R., and Sabatini, D.M. (2012). Amino acids and mTORC1: from lysosomes to disease. Trends Mol. Med. *18*, 524–533.

Efeyan, A., Zoncu, R., Chang, S., Gumper, I., Snitkin, H., Wolfson, R.L., Kirak, O., Sabatini, D.D., and Sabatini, D.M. (2013). Regulation of mTORC1 by the Rag GTPases is necessary for neonatal autophagy and survival. Nature *493*, 679–683.

Eichner, L.J., Brun, S.N., Herzig, S., Young, N.P., Curtis, S.D., Shackelford, D.B., Shokhirev, M.N., Leblanc, M., Vera, L.I., Hutchins, A., et al. (2019). Genetic Analysis Reveals AMPK Is Required to Support Tumor Growth in Murine Kras-Dependent Lung Cancer Models. Cell Metab. *29*, 285–302.e7.

Guida, M.C., Hermle, T., Graham, L.A., Hauser, V., Ryan, M., Stevens, T.H., and Simons, M. (2018). ATP6AP2 functions as a V-ATPase assembly factor in the endoplasmic reticulum. Mol. Biol. Cell *29*, 2156–2164.

Gwinn, D.M., Shackelford, D.B., Egan, D.F., Mihaylova, M.M., Mery, A., Vasquez, D.S., Turk, B.E., and Shaw, R.J. (2008). AMPK phosphorylation of raptor mediates a metabolic checkpoint. Mol. Cell *30*, 214–226.

Hardie, D.G. (2011). AMP-activated protein kinase: an energy sensor that regulates all aspects of cell function. Genes Dev. *25*, 1895–1908.

Hardie, D.G., and Lin, S.-C. (2017). AMP-activated protein kinase - not just an energy sensor. F1000Res. *6*, 1724.

Hardie, D.G., Ross, F.A., and Hawley, S.A. (2012). AMP-activated protein kinase: a target for drugs both ancient and modern. Chem. Biol. *19*, 1222–1236.

Hou, W., Han, J., Lu, C., Goldstein, L.A., and Rabinowich, H. (2010). Autophagic degradation of active caspase-8: a crosstalk mechanism between autophagy and apoptosis. Autophagy *6*, 891–900.

Hoxhaj, G., Najafov, A., Toth, R., Campbell, D.G., Prescott, A.R., and MacKintosh, C. (2012). ZNRF2 is released from membranes by growth factors and, together with ZNRF1, regulates the Na+/K+ATPase. J. Cell Sci. *125*, 4662–4675.

Please cite this article in press as: Najafov et al., RIPK1 Promotes Energy Sensing by the mTORC1 Pathway, Molecular Cell (2020), https://doi.org/10.1016/j.molcel.2020.11.008

Hoxhaj, G., Caddye, E., Najafov, A., Houde, V.P., Johnson, C., Dissanayake, K., Toth, R., Campbell, D.G., Prescott, A.R., and MacKintosh, C. (2016). The E3 ubiquitin ligase ZNRF2 is a substrate of mTORC1 and regulates its activation by amino acids. eLife *5*, e12278.

Hoxhaj, G., Hughes-Hallett, J., Timson, R.C., Ilagan, E., Yuan, M., Asara, J.M., Ben-Sahra, I., and Manning, B.D. (2017). The mTORC1 Signaling Network Senses Changes in Cellular Purine Nucleotide Levels. Cell Rep. *21*, 1331–1346.

Hsu, C.Y.M., and Uludağ, H. (2012). A simple and rapid nonviral approach to efficiently transfect primary tissue-derived cells using polyethylenimine. Nat. Protoc. *7*, 935–945.

Huang, J., and Manning, B.D. (2008). The TSC1-TSC2 complex: a molecular switchboard controlling cell growth. Biochem. J. *412*, 179–190.

Inoki, K., Zhu, T., and Guan, K.-L. (2003). TSC2 mediates cellular energy response to control cell growth and survival. Cell *115*, 577–590.

Kaiser, W.J., Daley-Bauer, L.P., Thapa, R.J., Mandal, P., Berger, S.B., Huang, C., Sundararajan, A., Guo, H., Roback, L., Speck, S.H., et al. (2014). RIP1 suppresses innate immune necrotic as well as apoptotic cell death during mammalian parturition. Proc. Natl. Acad. Sci. USA *111*, 7753–7758.

Kelliher, M.A., Grimm, S., Ishida, Y., Kuo, F., Stanger, B.Z., and Leder, P. (1998). The death domain kinase RIP mediates the TNF-induced NF-kappaB signal. Immunity *8*, 297–303.

Kuma, A., Hatano, M., Matsui, M., Yamamoto, A., Nakaya, H., Yoshimori, T., Ohsumi, Y., Tokuhisa, T., and Mizushima, N. (2004). The role of autophagy during the early neonatal starvation period. Nature *432*, 1032–1036.

Laplante, M., and Sabatini, D.M. (2012). mTOR signaling in growth control and disease. Cell *149*, 274–293.

Li, Y., Führer, M., Bahrami, E., Socha, P., Klaudel-Dreszler, M., Bouzidi, A., Liu, Y., Lehle, A.S., Magg, T., Hollizeck, S., et al. (2019). Human RIPK1 deficiency causes combined immunodeficiency and inflammatory bowel diseases. Proc. Natl. Acad. Sci. USA *116*, 970–975.

Lin, S.-C., and Hardie, D.G. (2018). AMPK: Sensing Glucose as well as Cellular Energy Status. Cell Metab. *27*, 299–313.

Long, B., Yin, C., Fan, Q., Yan, G., Wang, Z., Li, X., Chen, C., Yang, X., Liu, L., Zheng, Z., et al. (2016). Global Liver Proteome Analysis Using iTRAQ Reveals AMPK-mTOR-Autophagy Signaling Is Altered by Intrauterine Growth Restriction in Newborn Piglets. J. Proteome Res. *15*, 1262–1273.

Manning, B.D., Tee, A.R., Logsdon, M.N., Blenis, J., and Cantley, L.C. (2002). Identification of the tuberous sclerosis complex-2 tumor suppressor gene product tuberin as a target of the phosphoinositide 3-kinase/akt pathway. Mol. Cell *10*, 151–162.

Martinez, J., Cunha, L.D., Park, S., Yang, M., Lu, Q., Orchard, R., Li, Q.-Z., Yan, M., Janke, L., Guy, C., et al. (2016). Noncanonical autophagy inhibits the autoinflammatory, lupus-like response to dying cells. Nature *533*, 115–119.

Menon, S., Dibble, C.C., Talbott, G., Hoxhaj, G., Valvezan, A.J., Takahashi, H., Cantley, L.C., and Manning, B.D. (2014). Spatial control of the TSC complex integrates insulin and nutrient regulation of mTORC1 at the lysosome. Cell *156*, 771–785.

Mizushima, N., and Komatsu, M. (2011). Autophagy: renovation of cells and tissues. Cell *147*, 728–741.

Najafov, A., Sommer, E.M., Axten, J.M., Deyoung, M.P., and Alessi, D.R. (2011). Characterization of GSK2334470, a novel and highly specific inhibitor of PDK1. Biochem. J. *433*, 357–369.

Najafov, A., Shpiro, N., and Alessi, D.R. (2012). Akt is efficiently activated by PIF-pocket- and PtdIns(3,4,5)P3-dependent mechanisms leading to resistance to PDK1 inhibitors. Biochem. J. *448*, 285–295.

Najafov, A., Zervantonakis, I.K., Mookhtiar, A.K., Greninger, P., March, R.J., Egan, R.K., Luu, H.S., Stover, D.G., Matulonis, U.A., Benes, C.H., and Yuan, J. (2018). BRAF and AXL oncogenes drive RIPK3 expression loss in cancer. PLoS Biol. *16*, e2005756.

Najafov, A., Mookhtiar, A.K., Luu, H.S., Ordureau, A., Pan, H., Amin, P.P., Li, Y., Lu, Q., and Yuan, J. (2019). TAM kinases promote necroptosis by regulating oligomerization of MLKL. Mol. Cell *75*, 457–468.e4.

Ofengeim, D., and Yuan, J. (2013). Regulation of RIP1 kinase signalling at the crossroads of inflammation and cell death. Nat. Rev. Mol. Cell Biol. *14*, 727–736.

Papp, B., Pál, C., and Hurst, L.D. (2003). Dosage sensitivity and the evolution of gene families in yeast. Nature *424*, 194–197.

Peña-Llopis, S., Vega-Rubin-de-Celis, S., Schwartz, J.C., Wolff, N.C., Tran, T.A.T., Zou, L., Xie, X.-J., Corey, D.R., and Brugarolas, J. (2011). Regulation of TFEB and V-ATPases by mTORC1. EMBO J. *30*, 3242–3258.

Petzoldt, A.G., Gleixner, E.M., Fumagalli, A., Vaccari, T., and Simons, M. (2013). Elevated expression of the V-ATPase C subunit triggers JNK-dependent cell invasion and overgrowth in a Drosophila epithelium. Dis. Model. Mech. *6*, 689–700.

Polykratis, A., Hermance, N., Zelic, M., Roderick, J., Kim, C., Van, T.-M., Lee, T.H., Chan, F.K.M., Pasparakis, M., and Kelliher, M.A. (2014). Cutting edge: RIPK1 Kinase inactive mice are viable and protected from TNF-induced necroptosis in vivo. J. Immunol. *193*, 1539–1543.

Ran, F.A., Hsu, P.D., Wright, J., Agarwala, V., Scott, D.A., and Zhang, F. (2013). Genome engineering using the CRISPR-Cas9 system. Nat. Protoc. *8*, 2281–2308.

Rickard, J.A., O'Donnell, J.A., Evans, J.M., Lalaoui, N., Poh, A.R., Rogers, T., Vince, J.E., Lawlor, K.E., Ninnis, R.L., Anderton, H., et al. (2014). RIPK1 regulates RIPK3-MLKL-driven systemic inflammation and emergency hematopoiesis. Cell *157*, 1175–1188.

Rizzo, J.M., Tarsio, M., Martínez-Muñoz, G.A., and Kane, P.M. (2007). Diploids heterozygous for a vma13Delta mutation in Saccharomyces cerevisiae highlight the importance of V-ATPase subunit balance in supporting vacuolar acidification and silencing cytosolic V1-ATPase activity. J. Biol. Chem. *282*, 8521–8532.

Saxton, R.A., and Sabatini, D.M. (2017). mTOR Signaling in Growth, Metabolism, and Disease. Cell *168*, 960–976.

Schneider, C.A., Rasband, W.S., and Eliceiri, K.W. (2012). NIH Image to ImageJ: 25 years of image analysis. Nat. Methods *9*, 671–675.

Seo, J., Lee, E.-W., Sung, H., Seong, D., Dondelinger, Y., Shin, J., Jeong, M., Lee, H.-K., Kim, J.-H., Han, S.Y., et al. (2016). CHIP controls necroptosis through ubiquitylation- and lysosome-dependent degradation of RIPK3. Nat. Cell Biol. *18*, 291–302.

Settembre, C., Zoncu, R., Medina, D.L., Vetrini, F., Erdin, S., Erdin, S., Huynh, T., Ferron, M., Karsenty, G., Vellard, M.C., et al. (2012). A lysosome-to-nucleus signalling mechanism senses and regulates the lysosome via mTOR and TFEB. EMBO J. *31*, 1095–1108.

Shaw, R.J., Bardeesy, N., Manning, B.D., Lopez, L., Kosmatka, M., DePinho, R.A., and Cantley, L.C. (2004). The LKB1 tumor suppressor negatively regulates mTOR signaling. Cancer Cell *6*, 91–99.

Silke, J., Rickard, J.A., and Gerlic, M. (2015). The diverse role of RIP kinases in necroptosis and inflammation. Nat. Immunol. *16*, 689–697.

Stratigopoulos, G., De Rosa, M.C., LeDuc, C.A., Leibel, R.L., and Doege, C.A. (2018). DMSO increases efficiency of genome editing at two non-coding loci. PLoS ONE *13*, e0198637.

Sullivan, J.E., Brocklehurst, K.J., Marley, A.E., Carey, F., Carling, D., and Beri, R.K. (1994). Inhibition of lipolysis and lipogenesis in isolated rat adipocytes with AICAR, a cell-permeable activator of AMP-activated protein kinase. FEBS Lett. *353*, 33–36.

Takahashi, N., Duprez, L., Grootjans, S., Cauwels, A., Nerinckx, W., DuHadaway, J.B., Goossens, V., Roelandt, R., Van Hauwermeiren, F., Libert, C., et al. (2012). Necrostatin-1 analogues: critical issues on the specificity, activity and in vivo use in experimental disease models. Cell Death Dis. *3*, e437.

Teachey, D.T., Obzut, D.A., Axsom, K., Choi, J.K., Goldsmith, K.C., Hall, J., Hulitt, J., Manno, C.S., Maris, J.M., Rhodin, N., et al. (2006). Rapamycin improves lymphoproliferative disease in murine autoimmune lymphoproliferative syndrome (ALPS). Blood *108*, 1965–1971.

Tee, A.R., Fingar, D.C., Manning, B.D., Kwiatkowski, D.J., Cantley, L.C., and Blenis, J. (2002). Tuberous sclerosis complex-1 and -2 gene products function

Please cite this article in press as: Najafov et al., RIPK1 Promotes Energy Sensing by the mTORC1 Pathway, Molecular Cell (2020), https://doi.org/10.1016/j.molcel.2020.11.008

together to inhibit mammalian target of rapamycin (mTOR)-mediated downstream signaling. Proc. Natl. Acad. Sci. USA *99*, 13571–13576.

Ting, A.T., and Bertrand, M.J.M. (2016). More to Life than NF-κB in TNFR1 Signaling. Trends Immunol. *37*, 535–545.

Ting, A.T., Pimentel-Muiños, F.X., and Seed, B. (1996). RIP mediates tumor necrosis factor receptor 1 activation of NF-kappaB but not Fas/APO-1-initiated apoptosis. EMBO J. *15*, 6189–6196.

Truett, G.E., Heeger, P., Mynatt, R.L., Truett, A.A., Walker, J.A., and Warman, M.L. (2000). Preparation of PCR-quality mouse genomic DNA with hot sodium hydroxide and tris (HotSHOT). Biotechniques *29*, 52–54, 54.

Tummers, B., Mari, L., Guy, C.S., Heckmann, B.L., Rodriguez, D.A., Rühl, S., Moretti, J., Crawford, J.C., Fitzgerald, P., Kanneganti, T.-D., et al. (2020). Caspase-8-Dependent Inflammatory Responses Are Controlled by Its Adaptor, FADD, and Necroptosis. Immunity *52*, 994–1006.e8.

Wang, L., Du, F., and Wang, X. (2008). TNF-alpha induces two distinct caspase-8 activation pathways. Cell *133*, 693–703.

Yang, K., Neale, G., Green, D.R., He, W., and Chi, H. (2011). The tumor suppressor Tsc1 enforces quiescence of naive T cells to promote immune homeostasis and function. Nat. Immunol. *12*, 888–897.

Young, N.P., Kamireddy, A., Van Nostrand, J.L., Eichner, L.J., Shokhirev, M.N., Dayn, Y., and Shaw, R.J. (2016). AMPK governs lineage specification through Tfeb-dependent regulation of lysosomes. Genes Dev. *30*, 535–552.

Zhang, C.-S., Hawley, S.A., Zong, Y., Li, M., Wang, Z., Gray, A., Ma, T., Cui, J., Feng, J.-W., Zhu, M., et al. (2017). Fructose-1,6-bisphosphate and aldolase mediate glucose sensing by AMPK. Nature *548*, 112–116.

Zong, Y., Zhang, C.-S., Li, M., Wang, W., Wang, Z., Hawley, S.A., Ma, T., Feng, J.-W., Tian, X., Qi, Q., et al. (2019). Hierarchical activation of compartmentalized pools of AMPK depends on severity of nutrient or energy stress. Cell Res. *29*, 460–473.

Please cite this article in press as: Najafov et al., RIPK1 Promotes Energy Sensing by the mTORC1 Pathway, Molecular Cell (2020), https://doi.org/10.1016/j.molcel.2020.11.008

STAR★METHODS

KEY RESOURCES TABLE

REAGENT or RESOURCE	SOURCE	IDENTIFIER
Antibodies		
RIPK1	Cell Signaling	3493
RIPK1	In house	N/A
RIPK3 phospho-Ser227	Cell Signaling	93654
RIPK3	Abcam	ab56164
hCASP8	Cell Signaling	9746
mCASP8	Enzo Life Sciences	804-447-C100
hMLKL	Abcam	ab183770
mMLKL phospho-Ser345	Cell Signaling	37333
MLKL	In house	N/A
MLKL	Cell Signaling	14993
TSC2 phospho-Ser1387	Cell Signaling	5584
TSC2	Cell Signaling	4308
AMPK	Cell Signaling	5831
S6K phospho-Thr389	Cell Signaling	9205
S6K	Cell Signaling	2708
S6 phospho-Ser240/244	Cell Signaling	5364
S6	Cell Signaling	2317
ACC p-Ser79	Cell Signaling	3661
ACC	Cell Signaling	3662
4E-BP1 phospho-Thr37/46	Cell Signaling	2855
4E-BP1	Cell Signaling	9644
p62	Cell Signaling	5114
HK2	Cell Signaling	2867
Beta-Actin	Santa Cruz Biotech.	sc-1615
Tubulin	Sigma	T-9026
GAPDH	Cell Signaling	5174
S6 pS240-FITC	Miltenyi	130-106-603
ULK1 p-Ser757	Cell Signaling	14202
ULK1	Cell Signaling	8054
AMPK substrate motif antibody	Cell Signaling	5759
LAMP1	Abcam	ab25245
LAMP2	Santa Cruz Biotech.	Sc-71492
Raptor	Cell Signaling	2280
Raptor phospho-Ser792	Cell Signaling	2083
mTOR	Cell Signaling	2983
XIAP	Cell Signaling	2045
cIAP1	Cell Signaling	7065
TSC1	Cell Signaling	4906
Anti-K63 ubiquitin nanobody	Gift from Dr. Vishva Dixit	N/A
Anti-K48 ubiquitin nanobody	Gift from Dr. Vishva Dixit	N/A
Anti-M1 ubiquitin nanobody	Gift from Dr. Vishva Dixit	N/A
Chemicals, Peptides, and Recombinant Proteins		
TNFα	Cell Sciences	CRT192C
DMEM medium	Corning	10-017-CV

(*Continued on next page*)

Please cite this article in press as: Najafov et al., RIPK1 Promotes Energy Sensing by the mTORC1 Pathway, Molecular Cell (2020), https://doi.org/10.1016/j.molcel.2020.11.008

Continued

REAGENT or RESOURCE	SOURCE	IDENTIFIER
Glutathione Sepharose 4B	GE Healthcare	17-0756-01
McCoy's 5A medium	GIBCO	16600-082
SM-164	In house	N/A
PEI MAX (MW 40,000)	Polysciences	24765
Amphotericin B	Santa Cruz Biotech.	sc-202462A
ATP solution (100mM)	Sigma	A6559
zVAD.fmk	Sigma	V116
Anti-FLAG M2 Affinity Gel	Sigma	A2220
3X FLAG® Peptide	Sigma	F4799
Mouse TrueBlot® ULTRA	Rockland	18-8817-31
Rabbit TrueBlot®	Rockland	18-8816-31
Lipofectamine RNAiMAX	Thermo Scientific	13778-150
ProLong® Diamond Antifade with DAPI	Thermo Scientific	P36966
HEPES (1M, pH 7.4)	Thermo Scientific	15630080
Necrosulfonamide	Tocris	5025
Rapamycin	Cayman Chemical	13346
Nec-1 s	In house	N/A
GSK'840/843/872	Gift from Dr. Vishva Dixit	N/A
Torin-1	SelleckChem	S2827
MagicRed™ (Cathepsin B probe)	ImmunoChemistry Tech.	937
pHrodo™ (Acidity probe)	Thermo Fisher Scientific	P35373
LysoTracker™ Red DND-99	Thermo Fisher Scientific	L7528
Critical Commercial Assays		
Toxilight™	Lonza	LT07-117
CellTiterGlo®	Promega	G7571
Plasmid Maxi Kit	QIAGEN	12162
Experimental Models: Cell Lines		
HT-29 cells	ATCC	HTB-38
HEK293T cells	ATCC	CRL-11268
Jurkat cells	ATCC	TIB-152
RIPK1-deficient Jurkat cells	Gift from Dr. Brian Seed	Ting et al., 1996
MEFs	In house	N/A
AMPKα1/α2 dKO MEFs	Gift from Dr. Benoit Viollet	N/A
Experimental Models: Organisms/Strains		
RIPK1−/− mice	Gift from Dr. Michelle Kelliher	N/A
RIPK3−/− mice	Gift from Dr. Vishva Dixit	N/A
FADD−/− mice	Gift from Dr. Douglas Green	N/A
Atg5−/− mice	Riken	Q154543
C57BL/6N wild-type mice	Taconic Biosciences	B6NTac
Oligonucleotides		
hRIPK1 sgRNA	Integrated DNA Technologies	GATGAAATCCAGTGACTTCC
hTSC2 sgRNA	Integrated DNA Technologies	CAGACTCTGCAGGACATCCT
Primers for genotyping	Integrated DNA Technologies	see Table S3
Primers for qRT-PCR	Integrated DNA Technologies	see Table S4
Recombinant DNA		
pSpCas9(BB)-2A-Puro (pX459)	Addgene	#62988
pLenti-SV40 Large+small T-antigen	Addgene	#22298

(*Continued on next page*)

Please cite this article in press as: Najafov et al., RIPK1 Promotes Energy Sensing by the mTORC1 Pathway, Molecular Cell (2020), https://doi.org/10.1016/j.molcel.2020.11.008

Continued

REAGENT or RESOURCE	SOURCE	IDENTIFIER
pcDNA3.1	Thermo Scientific	V79020
pEBG	Addgene	#22227
Software and Algorithms		
ImageJ	Schneider et al., 2012	https://imagej.nih.gov/ij/
GraphPad Prism v7.0	N/A	https://www.graphpad.com/

RESOURCE AVAILABILITY

Lead Contact

Further information and requests for reagents may be directed to and will be fulfilled by the Lead Contact Junying Yuan (jyuan@hms.harvard.edu).

Materials Availability

All unique/stable reagents generated in this study are available from the Lead Contact with a completed Materials Transfer Agreement.

Data and Code Availability

This study did not generate any unique datasets or code.

EXPERIMENTAL MODEL AND SUBJECT DETAILS

Cell lines

HEK293T and MEF cells were grown in DMEM medium (Corning, 10-017-CV, with L-glutamine, with 4.5 g/L glucose, without pyruvate); HT-29 cells were grown in McCoy's 5A medium (GIBCO, 16600-082, with L-glutamine); Jurkat and RIPK1-deficient Jurkat cells were grown in RPMI medium (Corning, 10-040-CV, with L-glutamine). The basal media were supplemented with 10% FBS (Sigma), 1X penicillin/streptomycin (Life Technologies), and 1 μg/mL amphotericin B (Santa Cruz Biotechnology, sc-202462A). Primary MEFs were prepared by crossing RIPK1$^{+/-}$ mice and isolation of embryos at ~E12-13 developmental stage. MEFs were used as "primary MEFs" for the first 7 days in culture and then immortalized by transfection with a plasmid encoding both SV40 Large and Small antigens (pLenti CMV/TO SV40 small + Large T (w612-1) was a gift from Eric Campeau (Addgene plasmid #22298; http://addgene.org/22298; RRID:Addgene_22298) using Lipofectamine 3000 reagent or using the PEI method (Hsu and Uludağ, 2012). Cells were checked for mycoplasma contamination every 60 days, using MycoAlert Mycoplasma Detection Kit from Lonza (#LT07-318). A fresh aliquot of each cell line was thawed every month to maintain a low passage number of the cell lines used in the experiments. Cells were routinely passaged every 2-3 days and not allowed to grow to confluence.

Animal work

Mice were maintained in a pathogen-free environment. Experiments were conducted according to the protocols approved by the Harvard Medical School Animal Care Committee. Neonate pups were collected on the day of birth and tissues were lyzed using Polytron handheld homogenizer (VWR) in a lysis buffer containing 25 mM HEPES (pH 7.5), 0.2% NP-40, 1% Triton X-100, 120 mM NaCl, 0.27 M sucrose, 5 mM EDTA, 5 mM EGTA, 50 mM NaF, 10 mM b-glycerophosphate, 5 mM sodium pyrophosphate, 1 mM Na_3VO_4 (fresh), 0.1% BME (fresh), 1mM PMSF (fresh), 2X Complete protease inhibitor cocktail (Roche) and 1 μg/mL microcystin-LR. Littermates were used for comparison in all experiments. All mouse experiments were independently reproduced at least two times, and all experiments involved at least 2-3 mice per group.

Atg5$^{-/-}$ mice were purchased from Riken (Q154543, RBRC02231 B6;129-Atg5 < tm1Nmz >). For Atg5$^{-/-}$ neonatal lethality rescues crosses, Atg5$^{+/-}$RIPK3$^{+/-}$ self-crosses, and both Atg5$^{+/-}$FADD$^{+/-}$RIPK3$^{-/-}$ self-crosses and Atg5$^{+/-}$FADD$^{-/-}$RIPK3$^{-/-}$ self-crosses (data not shown) were attempted. Pups were monitored daily for survival for the first three weeks after birth (for potential partial protection of the neonatal lethality) and tailed and genotyped at the weaning age (three weeks). The following primers were used for Atg5 genotyping by a multiplex PCR reaction: ATG5 check 2: ACAACGTCGAGCACAGCTGCGCAAGG; ATG5 exon3-1: GAATATGAAGGCACACCCCTGAAATG; ATG5 short 2: GTACTGCATAATGGTTTAACTCTTGC. Expected PCR bands: Atg5-WT: 351bp; Atg5-KO: 574bp. RIPK3$^{-/-}$ mice were a kind gift from Vishva Dixit of Genentech. The following primers were used for RIPK3 genotyping by a multiplex PCR reaction: common_RIPK3_genotyping: CGCTTTAGAAGCCTTCAGGTTGAC; WT_RIPK3_genotyping: GCAGGCTCTGGTGACAAGATTCATGG; KO_RIPK3_genotyping: CCAGAGGCCACTTGTGTAGCG. Expected PCR bands: RIPK3-WT: 750bp; RIPK3-KO: 470bp.

FADD$^{-/-}$ mice were a kind gift from Douglas R. Green of St. Jude Children's Research Hospital. The following primers were used for FADD genotyping by a multiplex PCR reaction: FADDnull_161Fwd:GAAGAACGCCTCGGTGGCCGGACTGG; FADDnull_162-

Please cite this article in press as: Najafov et al., RIPK1 Promotes Energy Sensing by the mTORC1 Pathway, Molecular Cell (2020), https://doi.org/10.1016/j.molcel.2020.11.008

Rev1:GGAGCAGAGGTTCCGTAGATACAGA; FADDnull_163Rev2:AAGCGCATGCTCCAGACTGCCTTGGGAA. Expected PCR bands: FADD-WT: 360bp; FADD-KO: 300bp.

RIPK1$^{-/-}$ mice were a kind gift from Dr. Michelle Kelliher of UMass Medical School. The following primers were used for RIPK1 genotyping: 415-CTGCTAAAGCGCATGCTC; 425-TGTGTCAAGTCTCCCTGCAG; 426-CACGGTCCTTTTGCCCTG. Two separate PCR reactions were set up. For RIPK1-wild-type allele reaction, primers 425 and 426 were used. For RIPK1-KO allele reaction, primers 415 and 426 were used. Expected PCR bands: RIPK1-WT: 500bp; RIPK1-KO: 400bp.

METHOD DETAILS

Materials

Protein A/G-Sepharose and glutathione-Sepharose beads were from Pierce. Luminol (A8511), p-coumaric acid (C9008), Tween 20 detergent, as well as anti-Flag M2-agarose and anti-myc-agarose beads were from Sigma. DMSO (sc-20258) was from Santa Cruz Biotechnology. Lipofectamine 2000 and Lipofectamine 3000 transfection reagents were from Life Technologies. Chemicals and inhibitors were purchased from SelleckChem (A769662 (S2697), Torin-1 (S2827), Metformin (S1950)) and Cayman Chemical Company (Microcystin-LR (10007188), Rapamycin (13346)), Fisher (Sodium Hydroxide, Triton X-100, NP-40), ChemCruz (Tween 20, Glycerol), ChemExpress (MK-2206), Sigma (Glucose, SDS, NP-40, CCCP, Rapamycin, Cycloheximide, Percoll, Paraformaldehyde) and Toronto Research Chemicals Inc (AICAR). MagicRed was from ImmunoChemistry Technologies (cat #: 937) and pHrodo was from Thermo Fisher Scientific (P35373). MycoAlert Mycoplasma Detection Kit was from Lonza (cat #: LT07-318). PEI MAX (MW 40,000) was from Polysciences (cat #: 24765). The following antibodies were used in this study. RIPK1 (Cell Signaling Technology (CST), 3493; human and mouse); RIPK3 (Abcam, ab56164 [human and mouse; for immunofluorescence]; CST, 95702 [mouse; for western blotting]); p-hMLKL (S358) (Abcam, ab187091); hMLKL (Abcam, ab183770), p-mMLKL (Abcam, ab196436; CST, 37333), hCASP8 (CST, 9746), mCASP8 (Enzo Life Sciences, 804-447-C100), Tubulin (Sigma, T9026), Beta-actin (Santa Cruz Biotechnology, sc-81178), mTOR (CST, 2983), TSC2 p-Ser1387 (CST, 5584), TSC2 (CST, 4308), TSC1 (CST, 4906), TBC1D7 (CST, 14949), LAMP1 (Abcam, ab25245), LAMP2 (Santa Cruz Biotechnology, sc-71492), HK2 (CST, 2867), p62 (CST, 5114), GAPDH (CST, 5174), ACC (CST, 3662), ACC p-Ser79 (CST, 3661), AMPK (CST, 5831), S6K p-Thr389 (CST, 9205), S6K (CST, 2708), S6 p-Ser240/244 (CST, 5364), S6 (CST, 2317), ULK1 p-Ser757 (CST, 14202), ULK1 (CST, 8054), MLKL p-Ser358 (CST, 91689), MLKL (CST, 14993), RIPK3 p-Ser227 (CST, 93654), Raptor (CST, 2280), Raptor p-S792 (CST, 2083), phospho-4E-BP1 (Thr37/46) (CST, 2855), 4E-BP1 (CST, 9644), XIAP (CST, 2045), cIAP1 (CST, 7065), AMPK substrate motif (CST, 5759); Anti-S6 pS240-FITC, human (clone: REA420, Miltenyi, 130-106-603). Mouse and rabbit TrueBlot® ULTRA were from Rockland Immunochemicals, Inc. (cat #: 18-8817-30, 18-8816-33). Anti-mouse/human mouse monoclonal RIPK1 and MLKL antibodies were also generated in-house against bacterially-expressed kinase domain of human MLKL and intermediate domain of human RIPK1.

Molecular Cloning, Plasmids and qRT-PCR

Molecular cloning was done using New England Biolabs restriction enzymes and their T4 DNA ligase. RNA was isolated using RNeasy kit (QIAGEN) and cDNA synthesis was performed using RNA to cDNA EcoDry Premix (Double Primed) (Takara Bio). Quantitative real-time PCR was done using SYBR® Green Real-Time PCR Master Mix (Thermo Fisher Scientific), on QuantStudio 7 Flex Real-Time PCR System (Thermo Fisher Scientific). Primer sequences for the qRT-PCR experiments are given below: ACTIN_F (human/mouse): CATTGTTACCAACTGGGACG; ACTIN_R (human/mouse): CAGAGGCATACAGGGACAG; ATP6V0A2_F (human): AAGACCTTTGTGAAACGCAATGT; ATP6V0A2_R (human): AGGACACGATGGTGTACCCTT; ATP6V0A2_F (mouse): TGGTGCAGTTCCGAGACCT; ATP6V0A2_R (mouse): GCAGGGGAATATCAGCTCTGG; ATP6V0E1_F (human/mouse): CATTGTGATGAGCGTGTTCTGG; ATP6V0E1_R (human/mouse): AACTCCCCGGTTAGGACCCTTA; ATP6V0E2_F (human): TGCTGTTACCTCTTCTGGCTC; ATP6V0E2_R (human): GGAAGCGCACGTACCAGAT; ATP6V0E2_F (mouse): CCATCTTGGCCCAACTGAAC; ATP6V0E2_R (mouse): CCCACAGGAAACGCACGTA; ATP6V1A_F (human): GGGTGCAGCCATGTATGAG; ATP6V1A_R (human): TGCGAAGTACAGGATCTCCAA; ATP6V1A_F (mouse): GCATTGTAGGAGCAGTTTC; ATP6V1A_R (mouse): GAGCCAGTTGACAGAGGG; ATP6V1E2_F (human): CCCTGAGTGATGTCGATGTGA; ATP6V1E2_R (human): GACTTTCAGCCTCGCCTGATT; ATP6V1E2_F (mouse): GCCCTGACTGACATAGACGTG; ATP6V1E2_R (mouse): GTGATGCGAGCCTGGTTTC; ATP6V1H_F (mouse): CCAAGATGGACATTCGAGGTG; ATP6V1H_R (mouse): CACTTTGTTGGCACGAACTTC; ATP6V1H_F (human): GGAAGTGTCAGATGATCCCCA; ATP6V1H_R (human): CCGTTTGCCTCGTGGATAAT; CTSD_F (mouse): GCTTCCGGTCTTTGACAACCT; CTSD_R (mouse): CACCAAGCATTAGTTCTCCTCC; CTSD_F (human): AACTGCTGGACATCGCTTGCT; CTSD_R (human): CATTCTTCACGTAGGTGCTGGA; GAPDH_F (human/mouse): TGCACCACCAACTGCTTAGC; GAPDH_R (human/mouse): GGCATGGACTGTGGTCATGAG; Hexa_F (mouse): TGGCCCCAGTACATCCAAAC; Hexa_R (mouse): GGTTACGGTAGCGTCGAAAGG; Neu1_F (mouse): GTAGACACTTTCCGCATCCC; Neu1_R (mouse): CGATGAAGGCTGTAGAGGAC; Cd63_F (mouse): GAAGCAGGCCATTACCCATGA; Cd63_R (mouse): TGACTTCACCTGGTCTCTAAACA

For RNA isolation, cells were seeded into 6-well plates and harvested 24 h later at 60%–70% confluence in 350 μl of the RNeasy RLT buffer, and the manufacturer's protocol was followed. Rapamycin and Torin-1 treatments were done for 16 h using 0.25 μM of the compounds. 1 μg of isolated RNA was used for the cDNA synthesis in the EcoDry Premix tubes.

Human AMPK alpha1 was cloned into pcDNA3.1 plasmid, with an N-terminal Myc tag. The constitutively-activating Thr172Asp (T172D) mutation was introduced into the pcDNA3.1-Myc-AMPK plasmid using standard DpnI-based mutagenesis methods.

Please cite this article in press as: Najafov et al., RIPK1 Promotes Energy Sensing by the mTORC1 Pathway, Molecular Cell (2020), https://doi.org/10.1016/j.molcel.2020.11.008

DpnI was purchased from New England Biolabs. RIPK1 was cloned into pEBG plasmid, which has an N-terminal GST tag or pcDNA3.1 plasmid with an N-terminal HA tag. TSC2 was cloned into pcDNA3.1 plasmid with an N-terminal Flag-tag.

Plasmids were transformed into in-house-made chemically-competent DH5α *E. coli* cells. Plasmid purifications and extractions were performed using QIAprep Spin Miniprep Kit (QIAGEN), QIAquick Gel Extraction Kit (QIAGEN), and Plasmid Maxi or Midi kits (QIAGEN). Sequencing was done with an ABI3730xl DNA analyzer at the DNA Resource Core of Dana-Farber/Harvard Cancer Center (funded in part by NCI Cancer Center support grant 2P30CA006516-48).

Generation of RIPK1 knockout and TSC2 S1387E knock-in cell lines using CRISPR/cas9

sgRNA oligos, used for generation of CRISPR/Cas9-mediated knockout/knock-in cell lines, were cloned into pX459-Puro vector (Ran et al., 2013) (pSpCas9(BB)-2A-Puro (PX459) V2.0 was a gift from Feng Zhang (Addgene plasmid # 62988; http://addgene.org/62988; RRID:Addgene_62988)). The sgRNA sequences were: human RIPK1: GATGAAATCCAGTGACTTCC; human TSC2 (for S1387E knock-in): CAGACTCTGCAGGACATCCT. HT-29 cells were transfected with pX459-puro-sgRNA plasmids using Lipofectamine 2000, according to manufacturer's protocol, and 48 h post-transfection were switched to fresh medium containing 2 μg/mL puromycin, for 7 days. Individual clones were picked and analyzed by western blotting and sequencing for loss of expression and in-dels, respectively.

For the knock-in cell line generation, cells were treated with 1% DMSO for 24 h (Stratigopoulos et al., 2018), prior to transfection of the plasmid and a 120bp donor PCR amplicon corresponding to a region around S1387 (which was amplified from a previously S1387E mutagenized pcDNA3.1-TSC2 plasmid). Transfection was done as follows. Mix A: 125 μl OptiMEM + 2 μg pX459-TSC2-exon34-sgRNA plasmid + 3 μg S1387E PCR donor + 5 μl P3000. Mix B: 125 μl OptiMEM + 7.5 μl Lipofectamine 3000. Mixes A and B were combined, vortexed, and incubated at 25°C for 15min. The 250 μl transfection mix was delivered onto cells in 6-well plates at 80% confluence. 24 h later (1 day post-transfection), cells were expanded from each 6-well plate well into a 15cm dish. 24 h later (2 days post-transfection), fresh medium with puromycin (2.5 μg/mL) was added. 48 h later (4 days post-transfection), once again fresh medium with puromycin (2.5 μg/mL) was added. Seven days after transfection, cells were switched to puromycin-free medium and feed every two days until colonies formed (~2 weeks). Clones were duplicated in 12-well plates, and genomic DNA was isolated using the HotSHOT method (Truett et al., 2000) with amplification of the target region using EmeraldAmp® GT PCR Master Mix (Takara, RR310B), followed by PCR cleanup using ExoI and SAP treatment. 10 μl of the PCR products were treated with 2 μl of rSAP (NEB, M0371S) and 1 μl of ExoI nuclease (NEB, M0293S) for 30min at 37°C, followed by 20min incubation at 80°C. Sequencing of the PCR products was carried out with an ABI3730xl DNA analyzer at the DNA Resource Core of Dana-Farber/Harvard Cancer Center (funded in part by NCI Cancer Center support grant 2P30CA006516-48). The knock-in clones were analyzed by western blotting to ensure that unwanted frameshift mutation introduction did not produce knockouts instead of knock-ins.

Glucose starvation treatments

Cells were rinsed once with warm PBS and starved of glucose using glucose-free DMEM (Corning) and 10% dialyzed serum (Clontech) supplemented with 1X NEAA (Corning) and 1X Penicillin/Streptomycin. The untreated control cells received the same medium supplemented with 25mM glucose to ensure an equal amount/freshness of growth factors present in the old versus new medium.

Cell Lysis, Immunoprecipitation, and Immunoblotting

Cells were treated in no more than 16 h-old medium at 60%–70% confluence and rinsed with room temperature PBS. Cells were lyzed in 1X SDS-PAGE sample buffer (63mM Tris-HCl, pH 6.8, 2% SDS, 1% beta-mercaptoethanol, 0.01% BPB, 10% glycerol) containing 1μg/mL microcystin-LR and 50mM NaF inhibit phosphatases. Lysates were immediately heated at 95°C for 1min. Samples were sonicated to shear the genomic DNA or treated with Benzonase® (1:200) for 10min at 25°C. Total cell lysates (20-30 μg) or pull-down samples were heated at 90°C for 5min in 1-1.5X SDS-PAGE sample buffer, subjected to 8%–10% SDS-PAGE and then electro-transferred onto nitrocellulose membranes for 100-120 min at 0.4A current, with the wet transfer tank submerged in an ice-water bath. Membranes were blocked for 1 h in TBST buffer containing 5%–10% (w/v) skimmed milk and probed with the indicated antibodies in TBST containing 5% (w/v) BSA, for 16 h at 4°C. For p-mMLKL (Abcam, ab196436), this incubation step was done for 48 h to enhance the signal to noise ratio. Detection was performed using HRP-conjugated secondary antibodies (1 h, 25°C, 1:5000 diluted into TBST) and in-house-made chemiluminescence reagent (2.5 mM luminol, 0.4 mM p-coumaric acid, 100 mM Tris-HCl, pH 8.6, 0.018% H_2O_2, 2min, 25°C, freshly-made every two weeks). Samples were normalized to tubulin or beta-actin levels, where necessary, following quantification of the tubulin or beta-actin band intensities using ImageJ.

Cell lysis for immunoprecipitation experiments was done as described previously (Najafov et al., 2011). Cells in 15cm dishes were lyzed in freshly-made 0.75 mL NP-40 lysis buffer (25 mM HEPES (pH 7.5), 0.2% NP-40, 120 mM NaCl, 0.27 M sucrose, 5 mM EDTA, 5 mM EGTA, 50 mM NaF, 10 mM b-glycerophosphate, 5 mM sodium pyrophosphate, 2 mM Na_3VO_4 (fresh), 20mM NEM (fresh), 1mM PMSF (fresh), 2X Complete protease inhibitor cocktail (Roche)). The lysis buffer was not stored at 4°C for longer than 4 weeks. Cell scraping was done on ice, while cell washing with PBS (25ml per 15cm dish or 4ml per 6-well plate) was done at 25°C, in order to not activate AMPK by cold-induced stress. Cell lysates were cleared by centrifugation at 16,000xg for 15min at 4°C. Lysate protein concentrations were determined using the Bradford Protein Assay (Bio-Rad, #500-0006). To increase signal/noise ratio in the immunoprecipitation experiments, the cell lysates were filtered through a 0.45 μm acetate cellulose syringe filter, and beads were washed 5 times with 1ml lysis buffer. AMPK immunoprecipitation was done using AMPKα antibody #2532 (CST). RIPK1 immunoprecipitation

Please cite this article in press as: Najafov et al., RIPK1 Promotes Energy Sensing by the mTORC1 Pathway, Molecular Cell (2020), https://doi.org/10.1016/j.molcel.2020.11.008

was done using an in-house-made anti-human RIPK1 antibody (RIPK1-ID-15) raised against the intermediate region of RIPK1. GST-RIPK1, HA-RIPK1, Myc-AMPK, and Flag-TSC2 were purified separately by 48 h transient expression in HEK293T cells, as described previously (Najafov et al., 2012).

Protein purification and *in vitro* kinase assays

Plasmids were transfected into HEK293T cells at 50% confluence in 16-24 h-old medium (transfection per 15cm dish: 20 μg plasmid + 55 μl PEI + 1ml OptiMEM, incubate for 15-20 min at 25°C). Cells were lyzed 48 h later in 0.75 mL of NP-40 lysis buffer (NLB) (25 mM HEPES (pH 7.5), 0.2% NP-40, 120 mM NaCl, 0.27 M sucrose, 2 mM EDTA, 2 mM EGTA, 50 mM NaF, 10 mM beta-glycerophosphate, 5 mM Na- pyrophosphate, 5 mM Na-orthovanadate (added fresh), 0.1% BME (added fresh), 1mM PMSF (added fresh), 2X Complete protease inhibitor cocktail (Roche, added fresh)).

Proteins were bound to anti-Flag-M2-agarose or GSH-Sepharose beads for 4 h on a rotating wheel at 4°C. The beads were washed twice with NLB containing phosphatase inhibitors (each wash for 5min on a rotating wheel at 4°C) and twice with a wash buffer containing 1% Triton X-100, 250 mM NaCl, 25mM HEPES pH7.4. GST-tagged proteins were eluted with 20mM glutathione for 20min at 25°C. Flag-tagged proteins were eluted with 0.3 mg/mL Flag peptide for 2 h at 4°C, on a wheel.

In vitro kinase assays were performed as previously described (Najafov et al., 2011). Flag-RIPK1^{K45M}, Flag-TSC2, Flag-TSC1, and Myc-AMPK-alpha1^{T172D} were mixed at equimolar ratios in a kinase reaction buffer (25mM HEPES pH 7.4, 50 mM KCl, 10 mM $MgCl_2$, 2X Roche's EDTA-free protease inhibitor cocktail, 0.1% BME) and ATP was added to 200 μM final concentration. The reaction was terminated following 30min shaking at 1200rpm, at 30°C, by addition of 5X SDS-PAGE sample buffer and heating at 95°C for 5min.

Ubiquitin chain immunoprecipitation

For K63-linked ubiquitin chain immunoprecipitation, cells were lyzed in ULB (20 mM Tris-HCl, pH 7.5, 135 mM NaCl, 1.5 mM MgCl2,1 mM EGTA, 1% Triton X-100) freshly supplemented with 6M urea, 20mM NEM and 1mM PMSF. The protocol for immunoprecipitation was adapted from de Almagro et al. (de Almagro et al., 2015). The K63-, K48- and M1-specific nanobodies were a gift from Genentech. The final concentration of urea for M1 IPs was maintained at 6M, while it was decreased to 3M for K63 and K48 IPs. 3 μg of the antibodies were used per 15cm dish. Immunoprecipitations were carried out on a rotating wheel for 16 h at 4°C and 6 h at 25°C for K63/K48 and M1 IPs, respectively. 40 μl of protein A/G-Sepharose beads were used per IP, and the beads were washed three times using ULB freshly supplemented with 3M urea, 20mM NEM, and 1mM PMSF. Proteins were eluted using 2X SDS-PAGE sample buffer.

Light Microscopy

All the microscopy was performed at The Nikon Imaging Center at Harvard Medical School, as described previously (Hoxhaj et al., 2012). Cells were visualized live or fixed with 4% paraformaldehyde in PBS for 15min at room temperature. Cells were permeabilized with 0.05% Triton X-110 for 10 min at 25°C. Blocking was done with 1% BSA in PBS + 0.1% Tween 20 for 1 h at 25°C. Antibodies were diluted in fresh blocking buffer. Lysotracker staining was performed as per manufacturer's recommendations (Life Technologies). The following antibodies were used at the indicated dilutions: LAMP1 (1:100, Abcam, ab25245), LAMP2 (1:200, Santa Cruz Biotechnology, sc-71492). Secondary antibodies (AlexaFluor 488 and 594, Life Technologies) were diluted to 1:500 in the blocking buffer. Live cell imaging was done as described previously (Hoxhaj et al., 2016). All live-cell imaging experiments were done in 24-well glass-bottom plates (VWR, 82050-898) and in phenol-free complete DMEM media (GIBCO). Prior to live-cell imaging, Rapamycin or Torin-1 were freshly pre-diluted in phenol-free complete DMEM media and mixed with the medium in which cells were grown, at a 1:1 ratio, to achieve the final concentrations of 0.25 μM. Imaging was done on randomly-selected nine fields of view per treatment or slide. ProLong® Diamond Antifade Mountant with DAPI (Thermo) was used as a mounting medium. Slides were dried overnight at 25°C in the dark, sealed with nail polish, stored at 4°C imaged within 3 days.

Electron Microscopy and Lysosomal Size Measurements

Cells were fixed by adding the fixative solution (1.25% formaldehyde, 2.5% glutaraldehyde, and 0.03% picric acid in 0.1 M sodium cacodylate buffer, pH 7.4) directly to the cell medium at 1:1 ration and incubation at room temperature for 1 h. Embedding was done using 1% osmium tetroxide + 1.5% potassium ferrocyanide, followed by 1% uranyl acetate and dehydration. Transmission electron microscopy imaging was done using a Tecnai G^2 Spirit BioTWIN and AMT 2k CCD camera at Harvard Medical School Electron Microscopy Facility.

The lysosomal diameter was calculated using electron microscopy by drawing a line across the lysosomes and calculating each diameter according to the length of the scale bar, in microns. For oval-shaped lysosomes, the longest of the two diameters was used in calculations of the lysosomal diameter population mean. All measurements were done blindly. About 40 lysosomes were measured for each sample.

Cell growth and cell death assays

Crystal violet cell growth assays and cell death / cell survival assays were done as described previously (Najafov et al., 2012, 2018). For crystal violet assays, cells were grown in 12-well plates in triplicates per condition, for 72 h post-treatment. Cells were rinsed in 2ml 25°C PBS and fixed with 1ml of 4% PFA in PBS for 20min at 25°C. Following 2 rinses with 2ml 25°C PBS, cells were stained with

Please cite this article in press as: Najafov et al., RIPK1 Promotes Energy Sensing by the mTORC1 Pathway, Molecular Cell (2020), https://doi.org/10.1016/j.molcel.2020.11.008

0.5ml 0.1% crystal violet solution (in 10% ethanol) for 20min at 25°C on a shaker. Cells were rinsed twice with 2ml 25°C PBS and scanned. The dye was extracted using 1ml of 10% acetic acid for 20-30min at 25°C with mild agitation. The extracted dye was diluted 1:4-1:10, and OD595 was determined using Synergy 2 plate reader (Biotek) in plastic 96-well plates.

ToxiLight Non-destructive Cytotoxicity BioAssay (Lonza, LT07-117) was used for membrane permeabilization cell death assays (for proof-of-principle of lytic cell death), as per manufacturer's instructions. CellTiter-Glo® Luminescent Cell Viability Assay (Promega, G7570) was used to determine cell viability, as per manufacturer's instructions.

For Toxilight assays, 12.5 μl of the culture medium from 12-well plates was taken in triplicates and mixed with 12.5 μl of the reagent in white opaque 384-well plates. Following 5min of agitation in the Synergy 2 plate reader (Biotek), luminescence was measured at a sensitivity setting of 200, with an integration time of 0.2 s.

For CellTiterGlo® assays, the culture medium from 12-well plates was aspirated, and 300 μl of the reagent diluted 1:2 with DMEM was added onto the cells. Following 10min of agitation in the dark, 20 μl of the lysates were transferred into white opaque 384-well plates, and the luminescence was measured in the Synergy 2 plate reader (Biotek), at a sensitivity setting of 100, with an integration time of 0.2 s.

pHrodo staining and flow cytometry

Cells were treated for 16 h with rapamycin and stained for 30min with 1X pHrodo (Thermo Fisher Scientific, #P35373) staining solution at 37°C. Chloroquine control was added where indicated at 50 μM final concentration for 15min prior to pHrodo staining. Cells were fixed with 2%–4% paraformaldehyde for 20min at 25°C, in the dark. Cells rinsed twice with PBS and detached using trypsin/EDTA solution and mixed 1:1 with complete culture medium. Flow cytometry was done on FACSCalibur (BD Biosciences), using the FL-1 laser.

For p-S6-FITC FACS, cells were fixed in 10cm dishes at 80% confluence with 7ml cold 100% methanol at −20°C for 10min, rinsed with 10ml PBS and fixed for 20min with 7ml 10% neutral-buffered formalin (Sigma) at 25°C with mild agitation. Cells were rinsed 3 times with 10ml PBS and scraped into 5ml PBS. Cells were centrifuged at 1000xg for 3min at 25°C and resuspended in 1ml BBT buffer (0.1% Tween-20 + 5% BSA in PBS + 0.5mM MgCl2/$CaCl_2$). After 20min incubation on ice, cells were centrifuged as before and resuspended in 100 μl BBT containing 10 μl of p-S6-Ser240-FITC antibody (Miltenyi, #130-106-603). Following 30min incubation at 25°C in the dark, cells were diluted with 3ml BBT and centrifuged as before. Flow cytometry was done either on FACSCantoII (BD Biosciences) or FACSCalibur (BD Biosciences).

Cathepsin B Activity

Cells were treated with 1X MagicRed (ImmunoChemistry Technologies, #937) staining solution for 30min at 37°C. Cells were analyzed live on an inverted Nikon microscope using the TRITC filter. Images were quantified using ImageJ. For intestinal staining, 0.5cm-long large intestine fragments of neonatal mice were immersed into 1ml of complete DMEM and treated with 1X MagicRed staining solution for 30min at 37°C. Tissues were rinsed 2 times with PBS, fixed in 10% neutral-buffered formalin (Sigma) for 16 h at 25°C in the dark, transferred into 70% ethanol, and sectioned. Imaging was done as described previously (Hoxhaj et al., 2016).

QUANTIFICATION AND STATISTICAL ANALYSIS

For all experiments, unless otherwise indicated, n was at least 3. Statistical analyses were performed using GraphPad Prism 7 or Microsoft Excel. Data were analyzed using one-way analysis of variance (ANOVA) test with Bonferroni post-test for non-paired datasets. Student's t test was used for paired datasets.

Molecular Cell, Volume *81*

Supplemental Information

RIPK1 Promotes Energy Sensing by the mTORC1 Pathway

Ayaz Najafov, Hoang Son Luu, Adnan K. Mookhtiar, Lauren Mifflin, Hong-guang Xia, Palak P. Amin, Alban Ordureau, Huibing Wang, and Junying Yuan

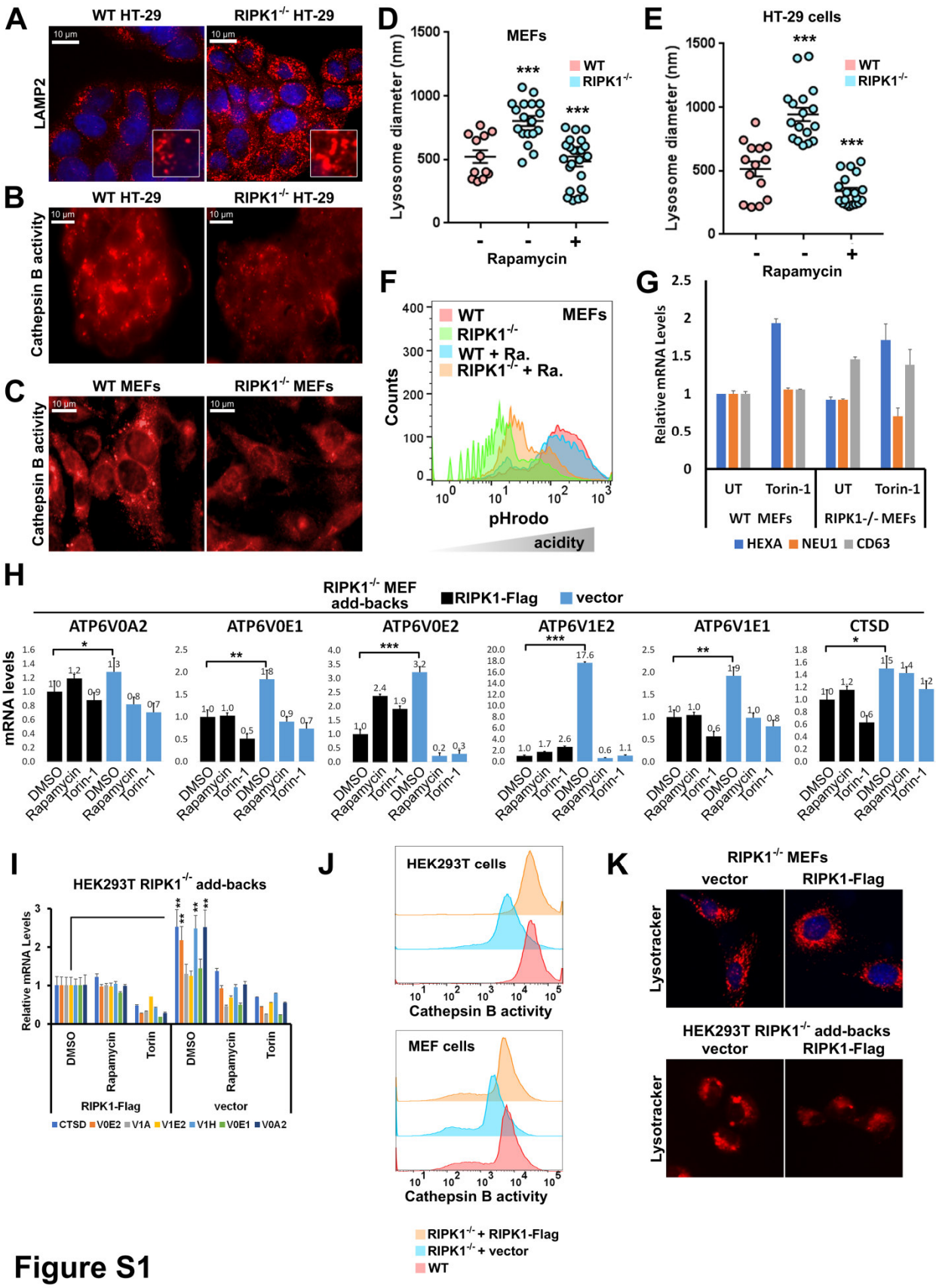
A
WT HT-29
RIPK1-/- HT-29
LAMP2
10 µm
B
Cathepsin B activity
C
WT MEFs
RIPK1-/- MEFs
D
MEFs
Lysosome diameter (nm)
WT
RIPK1-/-
***
Rapamycin
E
HT-29 cells
F
WT + Ra.
RIPK1-/- + Ra.
Counts
pHrodo
acidity
G
Relative mRNA Levels
UT
Torin-1
WT MEFs
RIPK1-/- MEFs
HEXA
NEU1
CD63
H
RIPK1-/- MEF add-backs
RIPK1-Flag
vector
ATP6V0A2
ATP6V0E1
ATP6V0E2
ATP6V1E2
ATP6V1E1
CTSD
mRNA levels
DMSO
Rapamycin
Torin-1
I
HEK293T RIPK1-/- add-backs
Relative mRNA Levels
Torin
RIPK1-Flag
vector
CTSD V0E2 V1A V1E2 V1H V0E1 V0A2
J
HEK293T cells
Cathepsin B activity
MEF cells
RIPK1-/- + RIPK1-Flag
RIPK1-/- + vector
WT
K
RIPK1-/- MEFs
vector
RIPK1-Flag
Lysotracker
HEK293T RIPK1-/- add-backs

Figure S1

Figure S1. RIPK1 loss leads to lysosomal defects. Related to Figure 1.

(A) Morphological defect of lysosomes in RIPK1$^{-/-}$ HT-29 cells. Cells were immunostained with LAMP2 antibody, counterstained with DAPI, and analyzed by fluorescence microscopy.

(B) Lysosomal activity defect in RIPK1$^{-/-}$ HT-29 cells as determined by the Magic Red™ Cathepsin B activity probe. Indicated cells were stained with Magic Red™.

(C) As in (B), except wild-type and RIPK1$^{-/-}$ MEFs were used.

(D) Rapamycin treatment rescues lysosomal enlargement, as a hallmark of dysfunctional lysosomes in RIPK1$^{-/-}$ MEFs, as determined by transmission electron microscopy (TEM). Cells were treated with rapamycin for 16h and fixed for TEM analysis. Quantification of the lysosomal diameter levels shown in (c) (n=60). Student's t-test was employed. Error bars: S.E.M.

(E) As in (E), except wild-type and RIPK1$^{-/-}$ HT-29 cells were used.

(F) Rapamycin treatment rescues low basal lysosomal acidity of RIPK1$^{-/-}$ cells. Wild-type and RIPK1$^{-/-}$ MEFs were treated with rapamycin for 16hrs, and live cells were stained with pHrodo® and analyzed by flow cytometry.

(G) As in Figure 1F, except HEXA, NEU1 and CD63 gene expression levels were analyzed, as representatives of lysosomal genes, expression of which does not increase in RIPK1 knockout background. Together with the non-stoichiometric increase in v-ATPase subunit expression, this data highlights a dysregulation in v-ATPase gene expression, rather than a general increase in lysosomal gene expression (see neonatal tissue data for these genes in Figure S14B).

(H) mTORC1-dependent lysosomal gene expression dysregulation in RIPK1$^{-/-}$ MEFs is rescued by re-expression of FLAG-mRIPK1. Cells were treated with either rapamycin or Torin-1 for 16 hours, and the expression of the indicated genes was analyzed by qRT-PCR.

(I) As in (A), except HEK293T RIPK1$^{-/-}$ monoclonal cell lines with stable expression of either empty vector or FLAG-hRIPK1 were used.

(J) MEF or HEK293T RIPK1$^{-/-}$ cell lines with stable expression of either empty vector or FLAG-hRIPK1 were used for cathepsin B activity assay using Magic Red™ probe and analyzed by flow cytometry.

(K) Morphological defect of lysosomes in RIPK1$^{-/-}$ MEF or HEK293T cells can be rescued by a stable re-expression of RIPK1. MEF or HEK293T RIPK1$^{-/-}$ cell lines with stable expression of either empty vector or FLAG-RIPK1 were stained using Lysotracker and analyzed by fluorescence microscopy. MEFs were fixed and counterstained with DAPI. HEK293T cells were analyzed live without counterstaining.

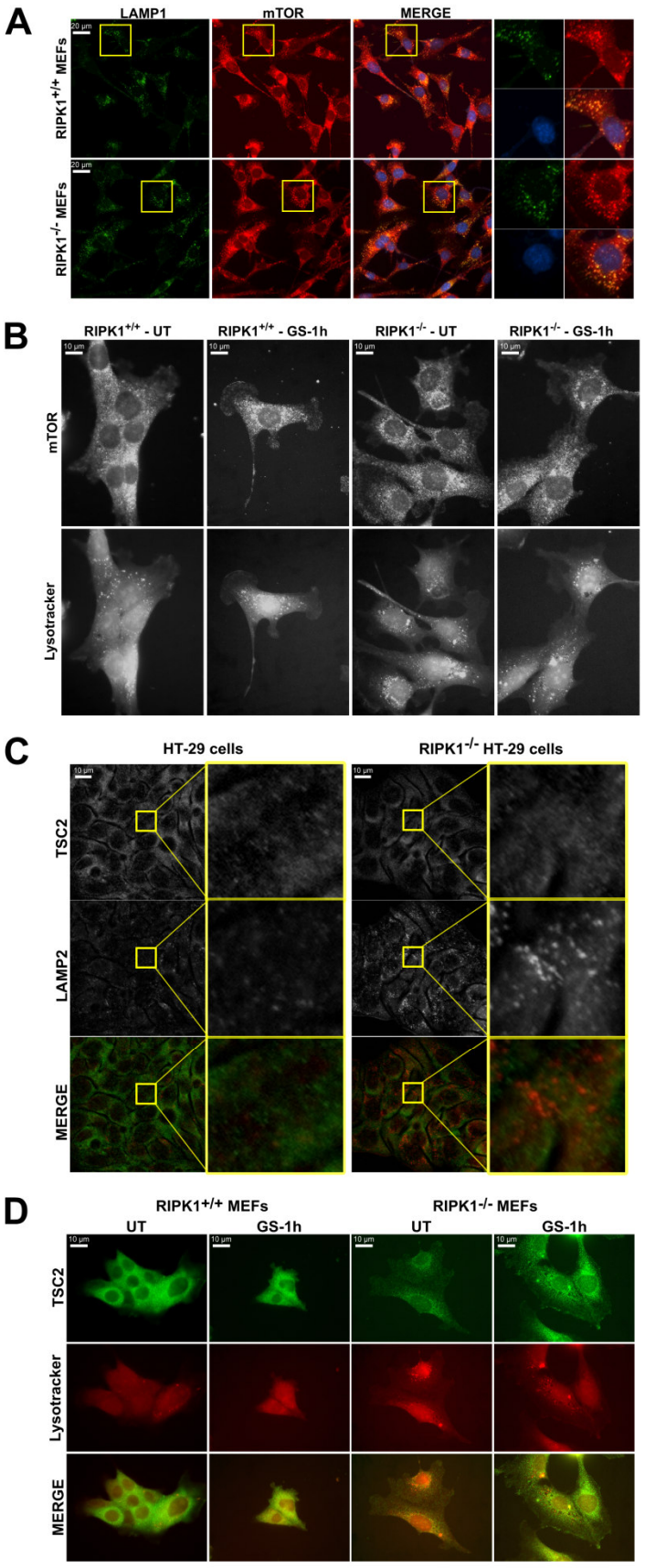
A
LAMP1
mTOR
MERGE
RIPK1+/+ MEFs
RIPK1-/- MEFs
B
RIPK1+/+ - UT
RIPK1+/+ - GS-1h
RIPK1-/- - UT
RIPK1-/- - GS-1h
mTOR
Lysotracker
C
HT-29 cells
RIPK1-/- HT-29 cells
TSC2
LAMP2
MERGE
D
RIPK1+/+ MEFs
RIPK1-/- MEFs
UT
GS-1h
UT
GS-1h
TSC2
Lysotracker
MERGE

Figure S2

Figure S2. RIPK1 loss does affect the subcellular localization of mTOR and TSC2. Related to Figure 1.

(A) Normal lysosomal localization of mTOR in wild-type versus RIPK1$^{-/-}$ cells. Indicated MEFs were used for immunofluorescence using LAMP1 and mTOR antibodies under normal serum conditions. Panels on the right show digitally magnified versions of the areas boxed in the main panels. Wild-type and RIPK1$^{-/-}$ cells with minimal difference in lysosomal size were selected for analysis to avoid lysosomal enlargement bias in RIPK1$^{-/-}$ cells.

(B) Normal lysosomal localization of mTOR in wild-type versus RIPK1$^{-/-}$ cells upon glucose starvation (GS) for 1hr. Indicated MEFs were used for immunofluorescence using LAMP1 and mTOR antibodies. Wild-type and RIPK1$^{-/-}$ cells with minimal difference in lysosomal size were selected for analysis to avoid lysosomal enlargement bias in RIPK1$^{-/-}$ cells.

(C) Normal cytosolic localization of TSC2 in wild-type versus RIPK1$^{-/-}$ cells. Indicated HT-29 cells were used for immunofluorescence using TSC2 and LAMP2 antibodies under normal serum conditions. Insets show digitally magnified versions of the areas boxed in the main panels. Wild-type and RIPK1$^{-/-}$ cells with minimal difference in lysosomal size were selected for analysis to avoid lysosomal enlargement bias in RIPK1$^{-/-}$ cells.

(D) Normal lysosomal localization of TSC2 in wild-type versus RIPK1$^{-/-}$ cells upon glucose starvation (GS) for 1hr. Indicated MEFs were used for immunofluorescence using Lysotracker and TSC2 antibodies. Wild-type and RIPK1$^{-/-}$ cells with minimal difference in lysosomal size were selected for analysis to avoid lysosomal enlargement bias in RIPK1$^{-/-}$ cells.

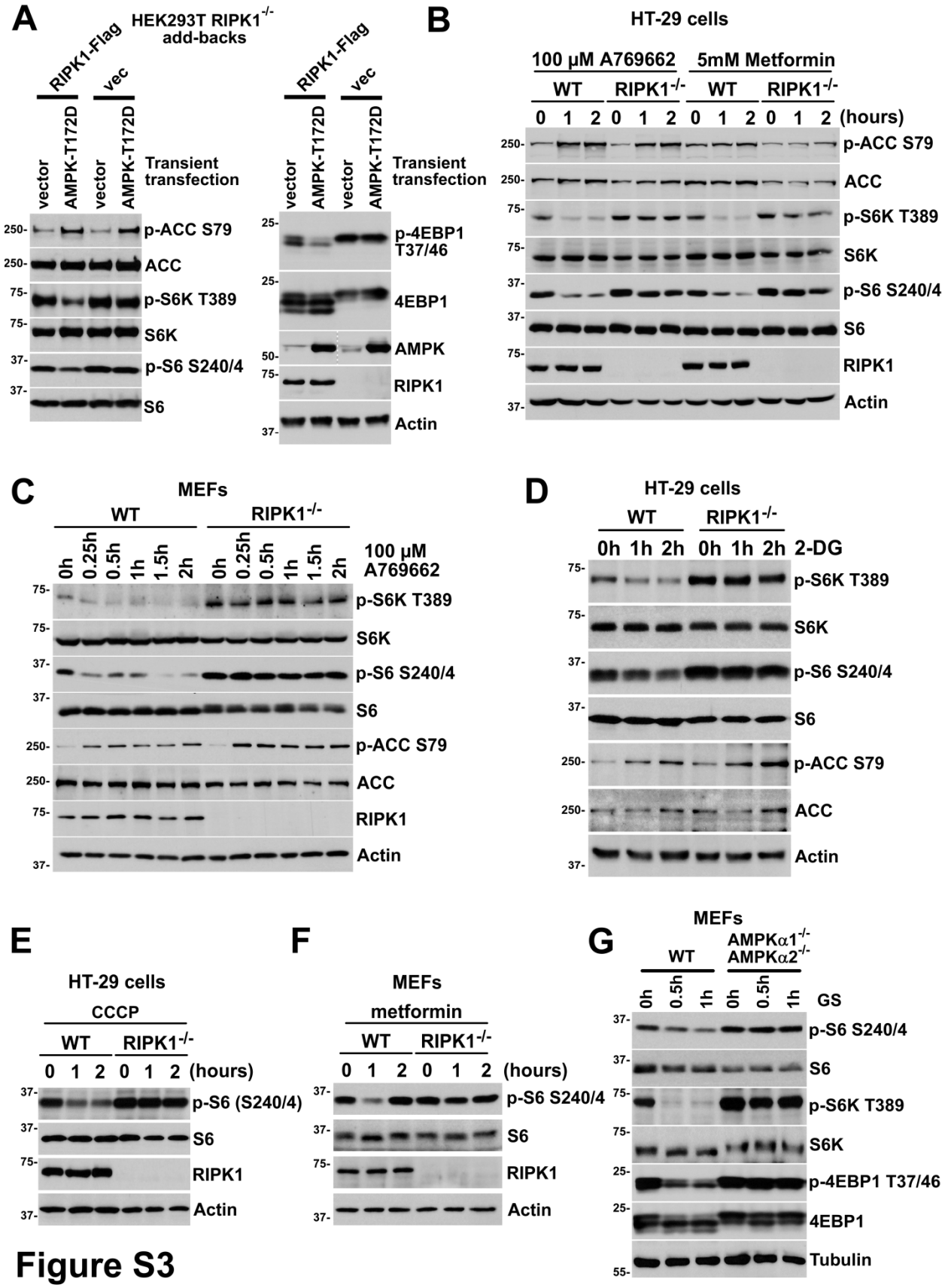
A
HEK293T RIPK1-/- add-backs
RIPK1-Flag
vec
vector
AMPK-T172D
Transient transfection
p-ACC S79
ACC
p-S6K T389
S6K
p-S6 S240/4
S6
p-4EBP1 T37/46
4EBP1
AMPK
RIPK1
Actin
B
HT-29 cells
100 μM A769662
5mM Metformin
WT
RIPK1-/-
(hours)
C
MEFs
100 μM A769662
D
HT-29 cells
2-DG
E
HT-29 cells
CCCP
p-S6 (S240/4)
F
MEFs
metformin
G
MEFs
AMPKα1-/- AMPKα2-/-
GS
Tubulin

Figure S3

Figure S3. RIPK1 is required for AMPK to inhibit mTORC1. Related to Figure 2.

(A) mTORC1 inhibition by overexpression of constitutively-active $AMPK^{T172D}$ is compromised in $RIPK1^{-/-}$ HEK293T cells indicating that these cells have defective signaling downstream of AMPK and upstream of mTORC1. The indicated add-backs in 6-well plates were transiently transfected with 2 µg of the indicated plasmids using Lipofectamine 3000 and harvested 24 hours later. Cell lysates were immunoblotted with indicated antibodies. Note that the AMPK blot has a deleted lane, but all lanes are from the same gel.

(B) mTORC1 inhibition upon activation of AMPK by 100 µM A769662 or 5 mM metformin is compromised in $RIPK1^{-/-}$ HT-29 cells. Cells were treated for the indicated time points, and cell lysates were immunoblotted with indicated antibodies.

(C) mTORC1 inhibition upon activation of AMPK by 100 µM A769662 is compromised in $RIPK1^{-/-}$ MEFs. Cell lysates were immunoblotted with indicated antibodies.

(D) mTORC1 inhibition upon activation of AMPK by HK2 inhibitor 1 mM 2-DG is compromised in $RIPK1^{-/-}$ HT-29 cells. Cell lysates were immunoblotted with indicated antibodies.

(E) mTORC1 inhibition upon activation of AMPK by 1 µM CCCP is compromised in $RIPK1^{-/-}$ HT-29 cells. Cell lysates were immunoblotted with indicated antibodies.

(F) mTORC1 inhibition upon activation of AMPK by 5 mM metformin is compromised in $RIPK1^{-/-}$ MEFs. Cell lysates were immunoblotted with indicated antibodies.

(G) mTORC1 inhibition upon activation of AMPK by glucose starvation is compromised in AMPK $\alpha1^{-/-}\alpha2^{-/-}$ MEFs. Cell lysates were immunoblotted with indicated antibodies.

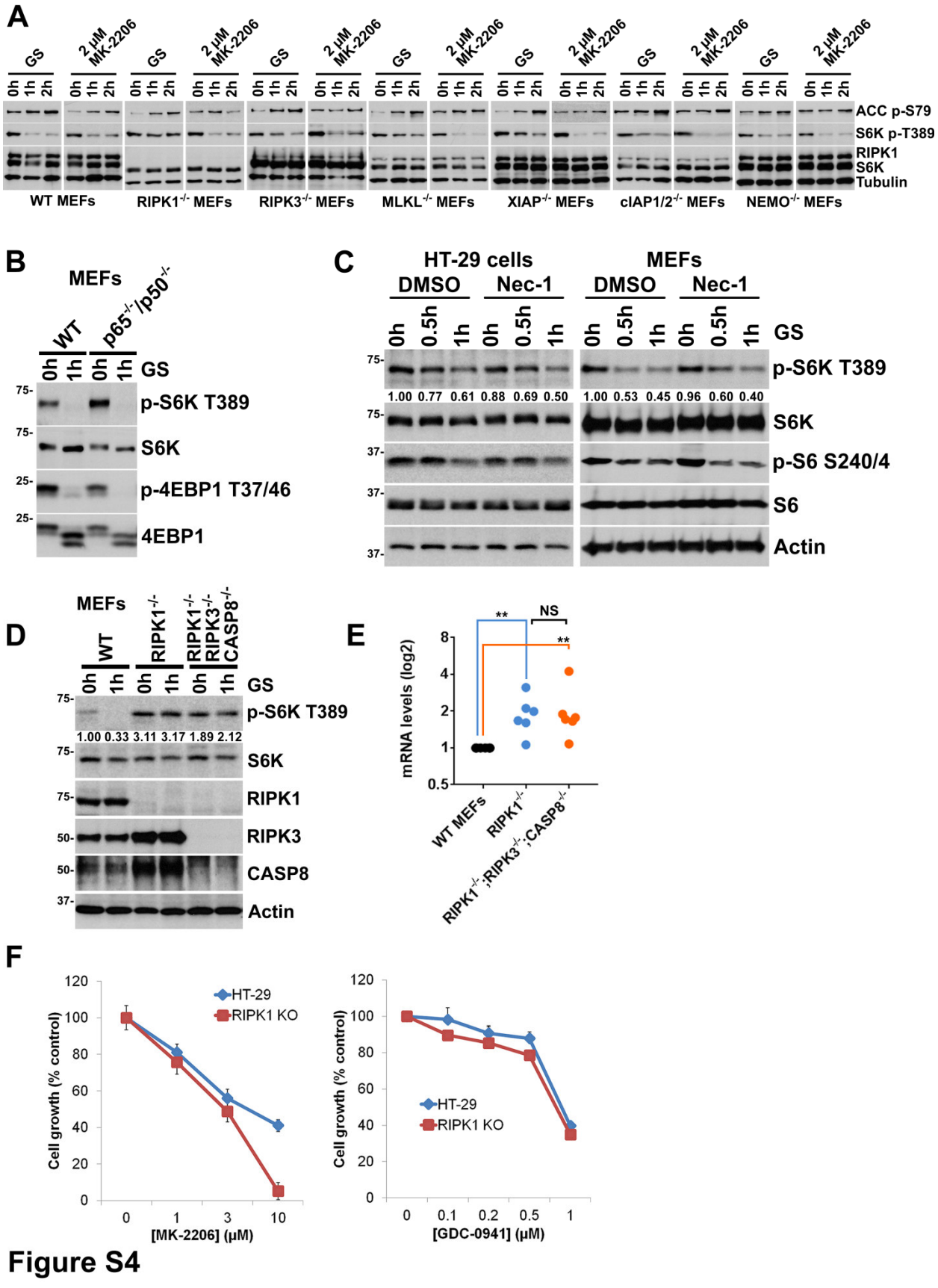
A
GS
2 μM MK-2206
0h 1h 2h
ACC p-S79
S6K p-T389
RIPK1
S6K
Tubulin
WT MEFs
RIPK1-/- MEFs
RIPK3-/- MEFs
MLKL-/- MEFs
XIAP-/- MEFs
cIAP1/2-/- MEFs
NEMO-/- MEFs
B
MEFs
WT
p65-/-/p50-/-
GS
p-S6K T389
S6K
p-4EBP1 T37/46
4EBP1
C
HT-29 cells
MEFs
DMSO
Nec-1
0h 0.5h 1h
GS
p-S6K T389
1.00 0.77 0.61 0.88 0.69 0.50
1.00 0.53 0.45 0.96 0.60 0.40
S6K
p-S6 S240/4
S6
Actin
D
MEFs
WT
RIPK1-/-
RIPK1-/- RIPK3-/- CASP8-/-
GS
p-S6K T389
1.00 0.33 3.11 3.17 1.89 2.12
S6K
RIPK1
RIPK3
CASP8
Actin
E
mRNA levels (log2)
**
NS
**
WT MEFs
RIPK1-/-
RIPK1-/-;RIPK3-/-;CASP8-/-
F
Cell growth (% control)
HT-29
RIPK1 KO
[MK-2206] (μM)
[GDC-0941] (μM)

Figure S4

Figure S4. The role of RIPK1 in promoting mTORC1 inhibition by AMPK is independent of the RIPK1-interacting TNFα receptor signaling components, the NF-κB pathway, and the RIPK3/CASP8 pro-death pathways. Related to Figure 3.

(A) mTORC1 inhibition upon activation of AMPK by glucose starvation is compromised in RIPK1$^{-/-}$, but not in RIPK3$^{-/-}$, MLKL$^{-/-}$, XIAP$^{-/-}$, cIAP1/2$^{-/-}$, or NEMO$^{-/-}$ MEFs, while all of the MEFs have normal mTORC1 inhibition upon inhibition of Akt by MK-2206. Cells were treated with glucose-free medium (GS) or MK-2206 for the indicated time points, and cell lysates were immunoblotted with indicated antibodies.

(B) mTORC1 inhibition upon activation of AMPK by glucose starvation is not compromised by NF-κB defective p65$^{-/-}$p50$^{-/-}$ MEFs.

(C) mTORC1 inhibition upon activation of AMPK by glucose starvation is not compromised by RIPK1 inhibitor Nec-1. Cells were pretreated with 25 μM Nec-1 for 30min and treated with the glucose-free medium as indicated. Cell lysates were immunoblotted with indicated antibodies. The values under the p-S6K panel indicate p-S6K / S6K quantification of the bands, with respect to the first lane.

(D) Knockout of RIPK3 and CASP8 does not rescue the inability of RIPK1$^{-/-}$ cells to inhibit mTORC1 following AMPK activation. Cells were glucose starved (GS) as indicated, and cell lysates were immunoblotted with indicated antibodies. Note that RIPK3 and CASP8 levels accumulate in RIPK1-/- cells, in agreement with the model (Figure S20). The values under the p-S6K panel indicate p-S6K / S6K quantification of the bands, with respect to the first lane.

(E) Knockout of RIPK3 and CASP8 does not rescue the dysregulated lysosomal gene expression in RIPK1$^{-/-}$. Cells were grown in normal medium, and RNA was isolated for qRT-PCR.

(F) RIPK1$^{-/-}$ HT-29 cells are not sensitized to Akt inhibitor MK-2206 or PI3K inhibitor GDC-0941, as judged by crystal violet cell proliferation assay. Cells were treated with the compounds at indicated concentrations for 3 days, and cell growth was determined using crystal violet assay.

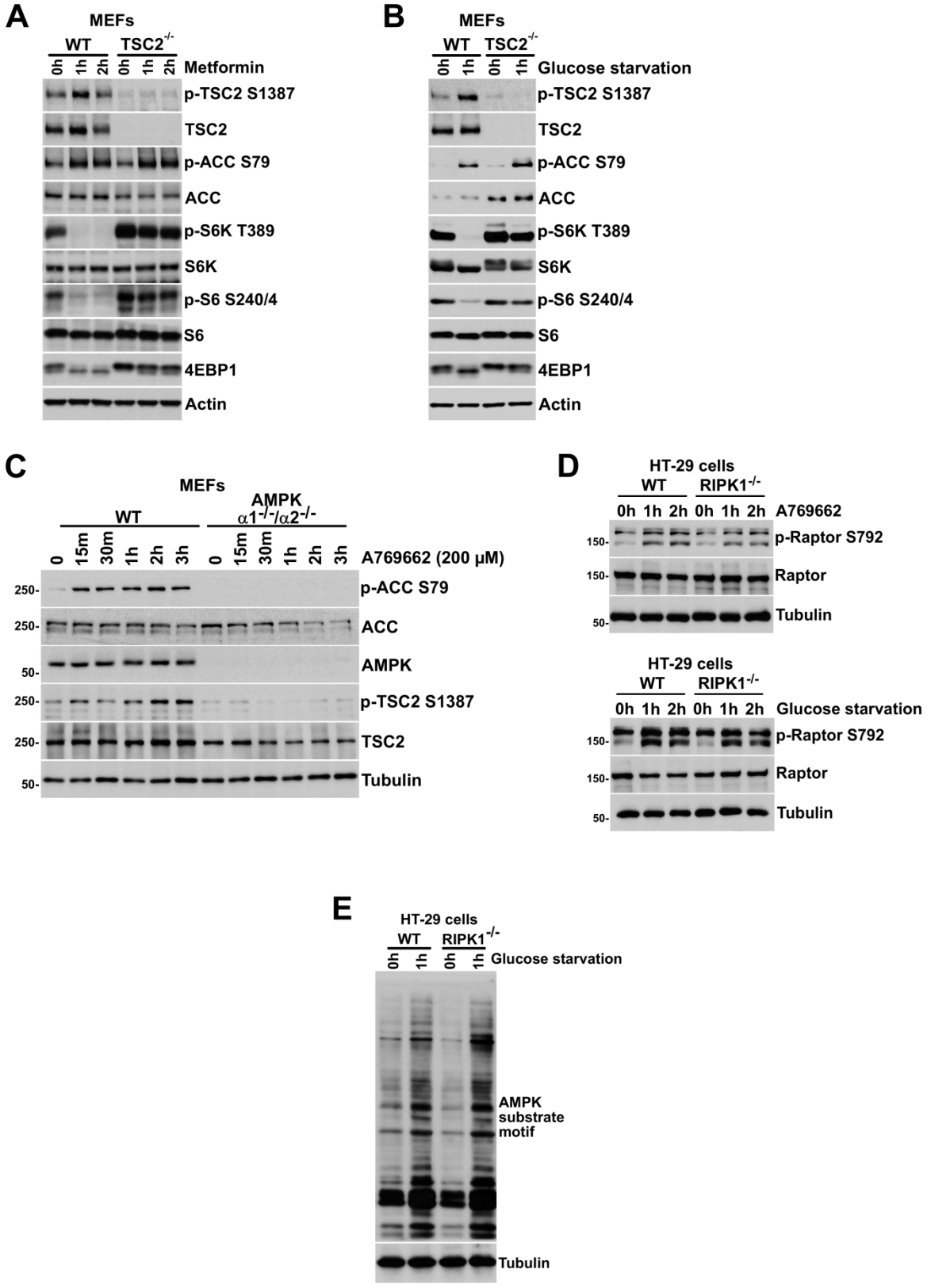
A
MEFs
WT
TSC2-/-
0h 1h 2h 0h 1h 2h
Metformin
p-TSC2 S1387
TSC2
p-ACC S79
ACC
p-S6K T389
S6K
p-S6 S240/4
S6
4EBP1
Actin
B
MEFs
WT
TSC2-/-
0h 1h 0h 1h
Glucose starvation
p-TSC2 S1387
TSC2
p-ACC S79
ACC
p-S6K T389
S6K
p-S6 S240/4
S6
4EBP1
Actin
C
MEFs
WT
AMPK α1-/-/α2-/-
0 15m 30m 1h 2h 3h 0 15m 30m 1h 2h 3h
A769662 (200 μM)
250-
p-ACC S79
250-
ACC
50-
AMPK
250-
p-TSC2 S1387
250-
TSC2
50-
Tubulin
D
HT-29 cells
WT
RIPK1-/-
0h 1h 2h 0h 1h 2h
A769662
150-
p-Raptor S792
150-
Raptor
50-
Tubulin
HT-29 cells
WT
RIPK1-/-
0h 1h 2h 0h 1h 2h
Glucose starvation
150-
p-Raptor S792
150-
Raptor
50-
Tubulin
E
HT-29 cells
WT
RIPK1-/-
0h 1h 0h 1h
Glucose starvation
AMPK substrate motif
Tubulin

Figure S5

Figure S5. mTORC1 inhibition by AMPK activation in TSC2-null and AMPK-null cells and the effect of RIPK1 loss on general AMPK activity. Related to Figure 4.

(A) TSC2 phosphorylation at Ser1387 in wild-type and $TSC2^{-/-}$ MEFs upon AMPK activation by 5 mM metformin treatment. Cells were treated as indicated, and cell lysates were immunoblotted with indicated antibodies. Note that, similar to that of $RIPK1^{-/-}$ cells, mTORC1 inhibition by AMPK activation is defective in $TSC2^{-/-}$ MEFs.

(B) As in (A), except AMPK was activated by glucose starvation.

(C) TSC2 phosphorylation at Ser1387 upon activation of AMPK by A769662 is compromised in AMPK α1-/-α2-/- MEFs. Cells were treated with 200 μM A769662, and cell lysates were immunoblotted with indicated antibodies.

(D) Raptor Ser792 phosphorylation by AMPK is not blocked in $RIPK1^{-/-}$ cells, unlike TSC2 Ser1387. Cells were treated as in Figure 2, and cell lysates were immunoblotted with indicated antibodies. **(E)** Phosphorylation of AMPK substrates is not affected in $RIPK1^{-/-}$ cells, as judged by the pan-AMPK substrate motif antibody. HT-29 cells were glucose-starved for 1h, and cell lysates were immunoblotted with indicated antibodies.

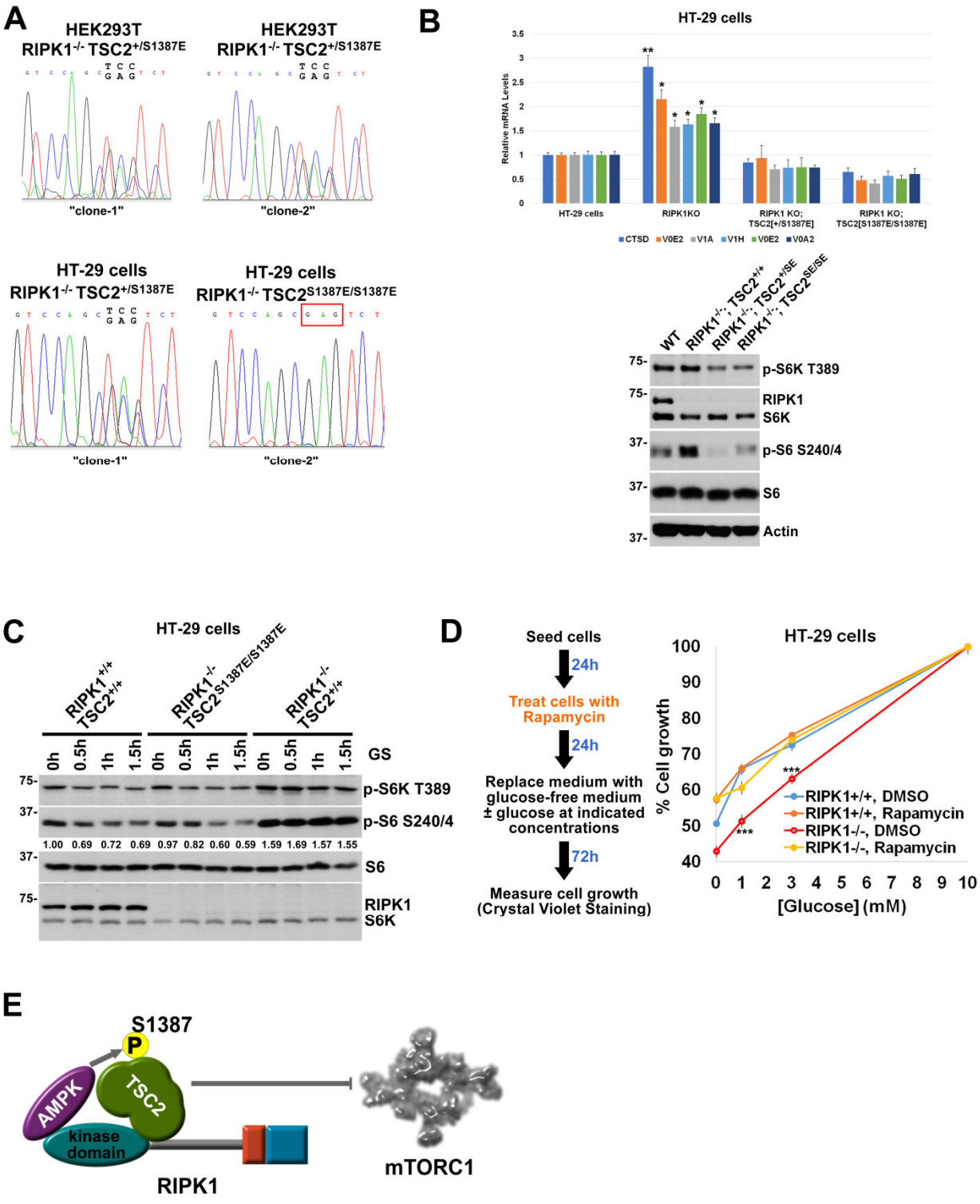
A
HEK293T RIPK1-/- TSC2+/S1387E
"clone-1"
HEK293T RIPK1-/- TSC2+/S1387E
"clone-2"
HT-29 cells RIPK1-/- TSC2+/S1387E
"clone-1"
HT-29 cells RIPK1-/- TSC2S1387E/S1387E
"clone-2"
B
HT-29 cells
Relative mRNA Levels
HT-29 cells
RIPK1KO
RIPK1 KO; TSC2[+/S1387E]
RIPK1 KO; TSC2[S1387E/S1387E]
CTSD V0E2 V1A V1H V0E2 V0A2
WT
RIPK1-/-; TSC2+/+
RIPK1-/-; TSC2+/SE
RIPK1-/-; TSC2SE/SE
p-S6K T389
RIPK1
S6K
p-S6 S240/4
S6
Actin
C
HT-29 cells
RIPK1+/+ TSC2+/+
RIPK1-/- TSC2S1387E/S1387E
RIPK1-/- TSC2+/+
0h 0.5h 1h 1.5h
GS
p-S6K T389
p-S6 S240/4
1.00 0.69 0.72 0.69 0.97 0.82 0.60 0.59 1.59 1.69 1.57 1.55
S6
RIPK1
S6K
D
Seed cells
24h
Treat cells with Rapamycin
24h
Replace medium with glucose-free medium ± glucose at indicated concentrations
72h
Measure cell growth (Crystal Violet Staining)
HT-29 cells
% Cell growth
[Glucose] (mM)
RIPK1+/+, DMSO
RIPK1+/+, Rapamycin
RIPK1-/-, DMSO
RIPK1-/-, Rapamycin
E
S1387
P
AMPK
TSC2
kinase domain
RIPK1
mTORC1

Figure S6

Figure S6. The effect of TSC2 S1387E knock-in and Rapamycin on the molecular and cellular effects of RIPK1 loss. Related to Figure 4.

(A) Sanger plots for the heterozygous and homozygous $TSC2^{S1387E}$ knock-in HEK293T and HT-29 clones used in Fig 3 and Figure S13.

(B) $TSC2^{S1387E}$ knock-in mutation rescues elevated lysosomal gene expression levels in $RIPK1^{-/-}$ HT-29 cells. Inset shows the changes in mTORC1 pathway activity in wild-type, $RIPK1^{-/-}$, and $RIPK1^{-/-}$;$TSC2^{S1387E}$ cells.

(C) $TSC2^{S1387E}$ knock-in mutation rescues the compromised mTORC1 inhibition upon AMPK activation in $RIPK1^{-/-}$ HT-29 cells. Cells were glucose starved (GS) as indicated, and cell lysates were immunoblotted with indicated antibodies. The values under the p-S6 panel indicate p-S6 / S6 quantification of the bands, with respect to the first lane.

(D) Rapamycin treatment rescues the defective growth of $RIPK1^{-/-}$ HT-29 cells under low glucose conditions. Cells were treated as indicated, and cell growth was assessed using the crystal violet assay.

(E) The model of the proposed role of RIPK1 in mediating AMPK-TSC2 interaction to promote mTORC1 inhibition.

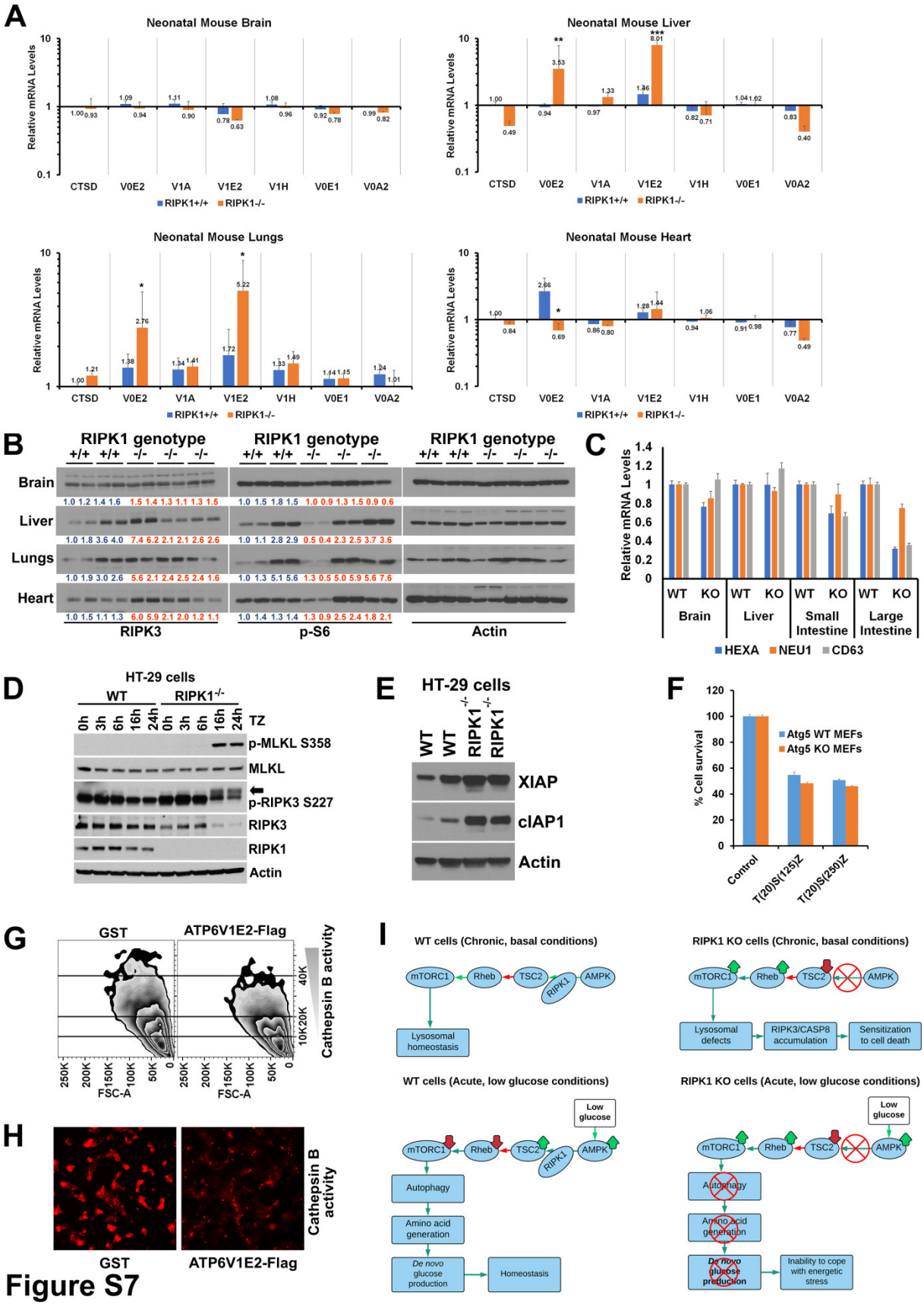
A
Neonatal Mouse Brain
Neonatal Mouse Liver
Neonatal Mouse Lungs
Neonatal Mouse Heart
Relative mRNA Levels
CTSD
V0E2
V1A
V1E2
V1H
V0E1
V0A2
RIPK1+/+
RIPK1-/-
B
RIPK1 genotype
+/+ +/+ -/- -/- -/-
Brain
Liver
Lungs
Heart
RIPK3
p-S6
Actin
C
Relative mRNA Levels
WT KO WT KO WT KO WT KO
Brain
Liver
Small Intestine
Large Intestine
HEXA
NEU1
CD63
D
HT-29 cells
WT
RIPK1-/-
0h 3h 6h 16h 24h 0h 3h 6h 16h 24h
TZ
p-MLKL S358
MLKL
p-RIPK3 S227
RIPK3
RIPK1
Actin
E
HT-29 cells
WT
WT
RIPK1-/-
RIPK1-/-
XIAP
cIAP1
Actin
F
% Cell survival
Atg5 WT MEFs
Atg5 KO MEFs
Control
T(20)S(125)Z
T(20)S(250)Z
G
GST
ATP6V1E2-Flag
Cathepsin B activity
FSC-A
H
GST
ATP6V1E2-Flag
Cathepsin B activity
I
WT cells (Chronic, basal conditions)
RIPK1 KO cells (Chronic, basal conditions)
WT cells (Acute, low glucose conditions)
RIPK1 KO cells (Acute, low glucose conditions)
mTORC1
Rheb
TSC2
RIPK1
AMPK
Low glucose
Lysosomal homeostasis
Lysosomal defects
RIPK3/CASP8 accumulation
Sensitization to cell death
Autophagy
Amino acid generation
De novo glucose production
Homeostasis
Inability to cope with energetic stress

Figure S7

Figure S7. Further characterization of the effect of RIPK1 loss on cells and neonatal mouse tissues. Related to Figures 6 and 7.

(A) Changes in the lysosomal gene expression in neonatal WT versus RIPK1$^{-/-}$ mouse tissues as judged by qRT-PCR analysis. Pups were collected on the day of birth, organs were harvested, and tails were genotyped. Note that the changes in the brain and heart are minimal, while the changes in the liver and lungs are significant. For simplicity of comparison expression of the indicated genes was normalized to the wild-type CTSD expression levels, following normalization to actin expression levels. RNA was isolated from at least 6 pups per genotype, and cDNA synthesis was performed without pooling the RNA from the pups. The qRT-PCR analysis was done one each pup separately for CTSD and the indicated v-ATPase subunits, which are known lysosomal genes. The tissue harvest and data analysis were blinded. The y-axis is on the log10 scale.

(B) RIPK3 and mTORC1 activity levels in neonatal mouse tissues. Indicated tissues were analyzed by western blotting using indicated antibodies. The values under the blots indicate quantification of the bands, normalized to actin and with respect to the first lane.

(C) As in Figure 4D, except HEXA, NEU1 and CD63 gene expression levels were analyzed, as representatives of lysosomal genes, expression of which does not increase in RIPK1 knockout background. Together with the non-stoichiometric increase in v-ATPase subunit expression, this data highlights a dysregulation in v-ATPase gene expression, rather than a general increase in lysosomal gene expression (related to Figure S3A).

(D) Necroptosis signaling turns on following TNFα + zVAD.fmk treatment of RIPK1-/-, but not wild-type HT-29 cells at later time points. Cells were treated with 50 ng/ml hTNFα + 30 μM zVAD.fmk for indicated time point and cell lysates were immunoblotted with indicated antibodies.

(E) Wild-type and RIPK1 knockout HT-29 cell lysates were probed using indicated antibodies.

(F) Loss of Atg5-driven autophagy does not affect sensitivity to necroptosis. MEFs were treated with TNFα and SM-164 at indicated concentrations in the presence of 20μM zVAD.fmk, and cell survival was assessed 16hrs later, using CellTiterGlo®.

(G) Overexpression of ATP6V1E2-Flag in HEK293T cells induces partial lysosomal defect, as judged by lower cathepsin B activity and less acidic pH. HEK293T cells were transiently (48h) transfected with either GST-expressing vector or ATP6V1E2-Flag subunit of the v-ATPase. Cathepsin B activity was assessed using MagicRed™ probe by flow cytometry.

(H) As in (C), except cells were analyzed using fluorescence microscopy.

(I) The proposed model of how RIPK1 loss results in an inability to cope with energetic stress and sensitization to cell death. Under chronic basal conditions, the basal mTORC1 levels are elevated in RIPK1$^{-/-}$ cells, due to the inability of basal AMPK activity to phosphorylate TSC2 and keep mTORC1 activity at normal levels. These abnormally high mTORC1 activity levels drive lysosomal defects, which result in RIPK3/CASP8 accumulation and sensitization to cell death. Under acute low energy conditions (e.g., glucose starvation), RIPK1$^{-/-}$ cells are unable to promote mTORC1 inhibition and induction of autophagy, since lysosomes are defective and since mTORC1 cannot be inhibited to induce autophagy (via the ULK1 pathway). This defect results in an inability to cope with energetic stress.

Table S1. The neonatal lethality of Atg5$^{-/-}$ mice does not depend on RIPK3-driven mechanisms. Atg5$^{+/-}$RIPK3$^{+/-}$ mice were crossed and pups were monitored for the first three weeks post-birth. Pups were genotyped at three weeks of age. Related to Figure 6.

Genotype	Expected	Observed
Atg5$^{-/-}$;RIPK3$^{-/-}$	6.00	0
Atg5$^{-/-}$;RIPK3$^{+/-}$	12.00	0
Atg5$^{-/-}$;RIPK3$^{+/+}$	6.00	0
Atg5$^{+/-}$;RIPK3$^{-/-}$	12.00	12
Atg5$^{+/-}$;RIPK3$^{+/-}$	24.00	36
Atg5$^{+/-}$;RIPK3$^{+/+}$	12.00	13
Atg5$^{+/+}$;RIPK3$^{-/-}$	6.00	8
Atg5$^{+/+}$;RIPK3$^{+/-}$	12.00	19
Atg5$^{+/+}$;RIPK3$^{+/+}$	6.00	8

Table S2. The neonatal lethality of Atg5$^{-/-}$ mice does not depend on RIPK3/FADD-driven mechanisms. Atg5$^{+/-}$FADD$^{+/-}$RIPK3$^{+/-}$ mice were crossed and pups were monitored for the first three weeks post-birth. Pups were genotyped at three weeks of age. Related to Figure 6.

Genotype	Expected	Observed
Atg5$^{-/-}$;FADD$^{-/-}$; RIPK3$^{-/-}$	9.3125	0
Atg5$^{-/-}$;FADD$^{+/-}$; RIPK3$^{-/-}$	18.625	0
Atg5$^{-/-}$;FADD$^{+/+}$; RIPK3$^{-/-}$	9.3125	0
Atg5$^{+/-}$;FADD$^{-/-}$; RIPK3$^{-/-}$	18.625	22
Atg5$^{+/-}$;FADD$^{+/-}$; RIPK3$^{-/-}$	37.25	49
Atg5$^{+/-}$;FADD$^{+/+}$; RIPK3$^{-/-}$	18.625	23
Atg5$^{+/+}$;FADD$^{-/-}$; RIPK3$^{-/-}$	9.3125	11
Atg5$^{+/+}$;FADD$^{+/-}$; RIPK3$^{-/-}$	18.625	29
Atg5$^{+/+}$;FADD$^{+/+}$; RIPK3$^{-/-}$	9.3125	15

Table S3. Primers for genotyping. Related to Figure 6, Table S1, and Table S2.

Primer name	Sequence
ATG5-check-2	ACAACGTCGAGCACAGCTGCGCAAGG
ATG5-exon3-1	GAATATGAAGGCACACCCCTGAAATG
ATG5-short-2	GTACTGCATAATGGTTTAACTCTTGC
RIPK3_common	CGCTTTAGAAGCCTTCAGGTTGAC
RIPK3_KO	CCAGAGGCCACTTGTGTAGCG
RIPK3_WT	GCAGGCTCTGGTGACAAGATTCATGG
FADDnull_161Fwd	GAAGAACGCCTCGGTGGCCGGACTGG
FADDnull_162Rev1	GGAGCAGAGGTTCCGTAGATACAGA
FADDnull_163Rev2	AAGCGCATGCTCCAGACTGCCTTGGGAA
RIPK1-415	CTGCTAAAGCGCATGCTC
RIPK1-425	TGTGTCAAGTCTCCCTGCAG
RIPK1-426	CACGGTCCTTTTGCCCTG

Table S4. Primers for qRT-PCR. Related to Figures 1, 4, 5, and 6.

Name	Species	Sequence
ACTIN_F	human + mouse	CATTGTTACCAACTGGGACG
ACTIN_R	human + mouse	CAGAGGCATACAGGGACAG
ATP6V0A2_F	human	AAGACCTTTGTGAAACGCAATGT
ATP6V0A2_R	human	AGGACACGATGGTGTACCCTT
ATP6V0A2_F	mouse	TGGTGCAGTTCCGAGACCT
ATP6V0A2_R	mouse	GCAGGGGAATATCAGCTCTGG
ATP6V0E1_F	human + mouse	CATTGTGATGAGCGTGTTCTGG
ATP6V0E1_R	human + mouse	AACTCCCCGGTTAGGACCCTTA
ATP6V0E2_F	human	TGCTGTTACCTCTTCTGGCTC
ATP6V0E2_R	human	GGAAGCGCACGTACCAGAT
ATP6V0E2_F	mouse	CCATCTTGGCCCAACTGAAC
ATP6V0E2_R	mouse	CCCACAGGAAACGCACGTA
ATP6V1A_F	human	GGGTGCAGCCATGTATGAG
ATP6V1A_R	human	TGCGAAGTACAGGATCTCCAA
ATP6V1A_F	mouse	GCATTGTAGGAGCAGTTTC
ATP6V1A_R	mouse	GAGCCAGTTGACAGAGGG
ATP6V1E2_F	human	CCCTGAGTGATGTCGATGTGA
ATP6V1E2_R	human	GACTTTCAGCCTCGCCTGATT
ATP6V1E2_F	mouse	GCCCTGACTGACATAGACGTG
ATP6V1E2_R	mouse	GTGATGCGAGCCTGGTTTC
ATP6V1H_F	mouse	CCAAGATGGACATTCGAGGTG
ATP6V1H_R	mouse	CACTTTGTTGGCACGAACTTC
ATP6V1H_F	human	GGAAGTGTCAGATGATCCCCA
ATP6V1H_R	human	CCGTTTGCCTCGTGGATAAT
CTSD_F	mouse	GCTTCCGGTCTTTGACAACCT
CTSD_R	mouse	CACCAAGCATTAGTTCTCCTCC
CTSD_F	human	AACTGCTGGACATCGCTTGCT
CTSD_R	human	CATTCTTCACGTAGGTGCTGGA
GAPDH_F	human + mouse	TGCACCACCAACTGCTTAGC
GAPDH_R	human + mouse	GGCATGGACTGTGGTCATGAG
Hexa_F	mouse	TGGCCCCAGTACATCCAAAC
Hexa_R	mouse	GGTTACGGTAGCGTCGAAAGG
Neu1_F	mouse	GTAGACACTTTCCGCATCCC
Neu1_R	mouse	CGATGAAGGCTGTAGAGGAC
Cd63_F	mouse	GAAGCAGGCCATTACCCATGA
Cd63_R	mouse	TGACTTCACCTGGTCTCTAAACA